Impacts of aerosol-monsoon interaction on rainfall and circulation over Northern India and the Himalaya Foothills

William K. M. Lau[1,2], Kyu-Myong Kim[3], Jainn-Jong Shi[4], T. Matsui[1], M. Chin[5], Qian Tan[5], C. Peters-Lidard[6], and W. K. Tao[7]

[1]*Earth System Science Interdisciplinary Center (ESSIC), U. of Maryland, College Park, Md 20740*
[2]*Department of Atmospheric Sciences, U. of Texas, Station College, TX, 77843.*
[3]*Climate and Radiation Laboratory, Earth Science Division, Goddard Space Flight Center, Greenbelt, MD, 20771*
[4] *Goddard Earth Science Technology, Application Research (GESTAR), Morgan State University, Baltimore, MD, 21251*
[5]*Atmospheric Chemistry and Dynamics Laboratory, Earth Science Division, Goddard Space Flight Center, Greenbelt, MD, 20771*
[6]*Earth Science Division, Goddard Space Flight Center, Greenbelt, MD, 20771*
[7]*Mesoscale Atmospheric Processes Laboratory, Earth Science Division, Goddard Space Flight Center, Greenbelt, MD., 20771*

Submitted to Climate Dynamics
July 20, 2016
Revised
October 17, 2016

Abstract

The boreal summer of 2008 was unusual for the Indian monsoon, featuring exceptional heavy loading of dust aerosols over the Arabian Sea and northern-central India, near normal all-India rainfall, but excessive heavy rain, causing disastrous flooding in the Northern Indian Himalaya Foothills (NIHF) regions, accompanied by persistent drought conditions in central and southern India. Using NASA Unified-physics Weather Research Forecast (NUWRF) model with fully interactive aerosol physics and dynamics, we carried out three sets of 7-day ensemble model forecast experiments: 1) control with no aerosol, 2) aerosol radiative effect only and 3) aerosol radiative and aerosol-cloud-microphysics effects, to study the impacts of aerosol-monsoon interactions on monsoon variability over the NIHF during the summer of 2008. Results show that aerosol-radiation interaction (ARI), *i.e.*, dust aerosol transport, and dynamical feedback processes induced by aerosol-radiative heating, plays a key role in altering the large-scale monsoon circulation system, reflected by an increased north-south tropospheric temperature gradient, a northward shift of heavy monsoon rainfall, advancing the monsoon onset by 1-5 days over the HF, consistent with the EHP hypothesis (Lau et al. 2006). Additionally, we found that dust aerosols, via the semi-direct effect, increase atmospheric stability, and cause the dissipation of a developing monsoon onset cyclone over northeastern India/northern Bay of Bengal. Eventually, in a matter of several days, ARI transforms the developing monsoon cyclone into meso-scale convective cells along the HF slopes. Aerosol-Cloud-microphysics Interaction (ACI) further enhances the ARI effect in invigorating the deep convection cells and speeding up the transformation processes. Results indicate that even in short-term (up to weekly) numerical forecasting of monsoon circulation and rainfall, effects of aerosol-monsoon interaction can be substantial and cannot be ignored.

1.Introduction

The Northern India and Himalayan foothills (NIHF) region is an essential component of the Indian monsoon (Gadgil et al. 2003). Summer monsoon rainfall over this region feeds the Ganges, and the Indus rivers, providing fresh water essential for agriculture, industrial and livelihood over hundreds of millions people in the region. The Himalayan foothills (HF), an escarpment that rises to over 5 km above the Indo-Gangetic Plain (IGP) over Northern India (NI), provides a major barrier to the northward advance of the Indian monsoon rainfall, as well as contributing to the thermal contrast between the Tibetan Plateau and the Indian Ocean (Boos and Kuang 2010; Wu et al. 2012). It also provides strong orographic forcing to the prevailing southwesterly monsoon flow, giving rise to strong vertical ascent and development of vigorous thunderstorm cells with intense precipitation during the monsoon season (Houze *et al*. 2007; Rasmusson and Houze 2012; Das *et al*. 2014). The importance of the NIHF orography in forcing strong convection and extreme precipitations, in relationship to the large-scale Indian monsoon has also been reported (Barros and Lang 2003; Barros and Lattenmaier 1994).

Recently, an increasing number of studies have suggested that absorbing aerosols (mainly desert dusts and carbonaceous aerosols) can affect the interannual and intraseasonal variability of the Indian monsoon rainfall (Lau et al. 2006; Lau and Kim 2006; Manoj et al. 2011; Hazra et al. 2013; Vinoj et al. 2014; Kim et al. 2015; D'Errico et al. 2015; Sanap and Pandithurai 2015, and many others). Based on these studies, Lau (2016) has proposed a new paradigm arguing that natural aerosol, particularly dust and carbonaceous aerosols from natural sources should be considered an essential component of an intrinsic aerosol-monsoon weather and climate system. Specifically for the NIHF region, the Elevated Heat Pump

77 (EHP) hypothesis (Lau et al. 2006) posited that through atmospheric diabatic heating and
78 circulation feedbacks, atmospheric heating due to absorbing aerosols from both
79 anthropogenic and natural sources accumulated over the Indo-Gangetic Plain during the pre-
80 monsoon period can, lead to increased rainfall and advance of the monsoon rainy season over
81 the NIHF. At present, effects of absorbing aerosols in increasing monsoon rainfall and
82 circulation consistent with EHP, but with significantly different regional spatial and temporal
83 details have been found in many global climate models (Lau et al. 2006; Meehl et al. 2008;
84 Randles and Ramawamy 2008; Wang et al. 2009; Collier and Zhang 2009; Henriksson, et al.
85 2014; D' Errico et al. 2015, Jin et al. 2015). One of the main reasons for the regional
86 differences is that state-of-the-art climate models, due to their coarse resolution generally, are
87 still unable to resolve the complex topography and interactions of monsoon winds,
88 precipitation and aerosol transport, sources and sink processes over the NIHF. For more
89 realistic simulations, the use of high-resolution regional atmospheric model with realistic
90 representation of aerosol and monsoon processes is required. In this paper, using the NASA
91 Unified Physics Weather Research Forecast (NU-WRF) model, we have carried out
92 numerical experiments aimed at providing a better understanding of the physical processes
93 involved in aerosol-monsoon interactions, including aerosol radiative and microphysical
94 effects, as well as induced dynamical feedbacks over the complex topography of the NIHF
95 region. The experiments will be conducted based on a case study of the 2008 Indian
96 monsoon.
97
98 *1.1 The 2008 Indian monsoon*

99 The all-Indian monsoon rainfall for the full monsoon season (June-September) during
100 2008 was near normal. However, rainfall was excessive in the north, but deficient in the
101 central and southern India for most of the season (Rao et al. 2011). Abnormally heavy rain
102 started in early June, and lasted through early August. The heavy rainfall eventually led to
103 the breaching of the Kosi river in early August, with disastrous flooding over Nepal and
104 many states in northern India including, Assam, Andhra Pradesh, Bihar, Maharashtra, Uttar
105 Pradesh, West Bengal and Orissa. The flood affected over 2.3 million people in the northern
106 part of the state of Bihar, prompting the Indian government to declare a national
107 disaster. The heavy rain in June (Fig. 1a) was found mainly over NIHF, extending
108 southeastward toward the Bay of Bengal. At the same time, rainfall was suppressed over
109 southwestern, central and southern, and extreme northeastern India. The summer of 2008
110 also witnessed an early onset of the monsoon over northern India (Tyagi et al. 2009). Most
111 interesting, it was also a year with unusually large loading of aerosols over the Arabian Sea,
112 northwestern India, and across central Indian during the early monsoon season (Fig. 1b). In
113 this study, we will examine the possible roles of aerosols in influencing this rather unusual
114 Indian monsoon.
115
116 **2. Modeling strategy and methodology**
117 We use the NASA Unified physics Weather Research Forecast (NUWRF)
118 regional atmospheric model to carry out ensemble forecast experiments to investigate the
119 role of aerosol-monsoon dynamic interaction in the NIHF region. NUWRF has been
120 developed at GSFC to unify physics in WRF with NASA's current physics package for
121 aerosol and cloud microphysics, as well as assimilation systems, common to GEOS-5, the

122 Goddard Cumulus Ensemble cloud model (GCE) (Tao et al. 2009), the Goddard
123 Chemistry and Radiation Transport (GOCART) model (Chin et al. 2004, 2009, 2014,
124 Ginoux et al. 2001), and the Land data Information System (LIS) (Peters-Lidard et al.
125 2007, 2015, Tao et al. 2013, Lang et al. 2014, Shi et al. 2014). Briefly, GOCART uses
126 the following modules in aerosol simulation: emission, which includes dust, sulfur, black
127 carbon, organic carbon, and sea-salt emissions; chemistry, which includes in-air and in-
128 cloud oxidations of sulfate precursors (SO_2 and DMS); turbulent dry deposition, which is
129 calculated by aerodynamic resistance; gravitational settling, which is a function of air
130 viscosity and particle size; and wet deposition, which accounts for the scavenging of
131 soluble species in convective updrafts and rainout/washout in large-scale precipitation.
132 Dust size distribution is calculated by solving the continuity equation for eight size bins
133 ranging from 0.1 to 10 μm in radii, representing mineral dust types from fine clay to
134 coarse sand particles. The continuity equation includes macroscopic advection by winds,
135 parameterized eddy diffusion and moist convection. The removal mechanisms include
136 dry deposition at the surface by impaction, wet deposition in and below clouds, and
137 gravitational settling. Dust emission is computed as a function of the surface wind at 10
138 m, a threshold frictional velocity, and a source function which is depended on
139 geographic locations and dust sizes (Ginaux et al. 2001, Gillette and Passi 1988).
140 For aerosol-cloud microphysics, NUWRF computes cloud droplet concentration
141 using aerosol mass directly predicted by GOCART/WRF-Chem at each time step. For a
142 given air temperature and supersaturation, cloud condensation nuclei (CCN) is calculated
143 from the aerosol species predicted by GOCART based on the Koehler curve (Koehler et al.
144 2006, Andreae and Rosenfeld 2008), while the concentration of ice nuclei (IN) is obtained

145 following the approach of DeMott et al. (2010). Both CCN and IN are diagnostic parameters
146 calculated from the WRF-Chem/GOCART-predicted aerosol mass concentrations in the
147 Goddard one-moment microphysics scheme. CCN is used to calculate the auto-conversion
148 of cloud liquid water (Qc) to rain water (Qr) following Liu and Daum (2004), while IN is
149 used to calculate 1) the conversion of cloud ice (Qi) to snow (Qs) due to the Bergeron
150 process and 2) the growth of cloud liquid water (Qc) to cloud ice (Qi) due to deposition.
151 The NUWRF team has also coupled GOCART with LIS which provides key
152 information (e.g., soil moisture and soil porosity) that GOCART uses to calculate dust
153 emissions. GOCART has also been coupled with the Goddard radiation and microphysics
154 scheme to simulate the direct and indirect aerosol effects on energy budget, cloud, and
155 precipitation. Parameterization schemes to estimate biogenic secondary organic aerosols have
156 also been integrated from WRF/Chem into NUWRF. In addition, several model utilities
157 have been developed and modified to facilitate NUWRF applications, including
158 implementation of time varying GOCART aerosols types and distribution as initial and
159 boundary conditions, and incorporation of pollutant emissions inventories for both
160 anthropogenic and natural sources. For the present experiments, the single scattering albedo
161 of dust aerosol at the visible band (0.4-0.7 μm) were specified in the range 0.95 to 0.79,
162 representing 8 size categories of dust from fine clay to coarse dust particles. The much
163 higher absorption (lower single scattering albedo) for larger size particles is consistent with
164 recent observations indicating coating of fine black carbon particle on the larger size sand
165 particles in Asian monsoon regions (Ganguly et al., 2005, Satheesh and Ramanathan 2008,
166 Eck et al., 2010)

For our model experiments, we followed the ensemble forecast methodology commonly used for monsoon numerical weather prediction up to a week to investigate the impacts of aerosol-monsoon dynamic interaction on short time scales. We used nested domains with 9 km resolution in an inner domain (60-100^{o}E, 10-40^{o}N) covering the Indian subcontinent and eastern Indo-China, and an outer domain with 27 km resolution, spanning the large-scale monsoon domain (40-120^{o} E, 5^{o}S-40^{o}N), with 61 layers in the vertical (Fig. S1). We selected the early monsoon period June 1- July 15 2008 for our study. This period covered the monsoon onset transition phase (June 11-17), and several subsequent heavy rain events over NIHF (See discussion in Section 2.1). We carried out 45, 7-day forecast experiments forced by prescribed observed sea surface temperature, at intervals of one day starting from June 1, first with no aerosol (NA) effects, which is still the common practice for most numerical weather forecasts in monsoon regions (Krishnamurti et al. 1991). A second identical set of experiments was carried out but with the inclusion of aerosol radiative (RAD) effect. A third set of experiments same as the control, except with both aerosol radiative and microphysics interactive effects (RADM) were carried out for the onset period June 11- 17. Initial and boundary conditions for meteorology and aerosols were obtained respectively from NCEP GFS 1^{o} x1^{o} global analysis, and from GOCART. By comparing the RAD and RADM to NA forecasts over the NIHF region in a realistic setting with a high-resolution regional model and sophisticated aerosol physics, we can gain a better understanding of intrinsic, aerosol-monsoon interaction for the Indian monsoon, involving no change in anthropogenic aerosol emissions. In following discussions, all model anomaly quantities are defined with respect to NA. For brevity, we shall refer to RAD anomalies as due to Aerosol-Radiative Interaction (ARI) effects. Effects of Aerosol-Cloud-microphysics-Interaction

190 (ACI) will be diagnosed from comparison between RADM and RAD anomalies. Aerosol
191 impacts will be examined using two different kinds of averaging. First, ensemble forecast
192 averaging for day-1 through day-7 for a specific date, will be compared to observation to
193 assess aerosol impacts on forecast skills. Second, ensemble averages of all forecasts as a
194 function of forecast days, will be used to assess the aerosol impact as a function of forecast
195 lead time. For comparing model results to observations, we use rainfall data from the
196 Tropical Precipitation Measuring Mission (TRMM), and winds and temperature data from
197 the NASA MERRA2, Modern Era Retrospective analysis for Research and Applications -
198 version 2 (Bosilovich et al. 2015).
199
200 **3. Results**
201 To facilitate comparison of model results to observations, and set the stage for the
202 model output analysis, a brief description of the observed large-scale features of the Indian
203 monsoon of 2008 is presented first.
204 *3.1 Observed large-scale monsoon features during June 2008*
205 The excessive rainfall over northern India in June 2008 (see Fig. 1) was accompanied
206 by an upper tropospheric (500-200 hPa) anomalous warming (deviation from climatological
207 mean) northwest of the Indian subcontinent, and an anomalous large-scale anticyclone (Fig.
208 2a), with strong easterlies over northern Indian and the Arabian Sea (20-35 N), consistent
209 with thermal wind balance in an environment with positive temperature gradient (warmer-
210 north and colder-south). The importance of the tropospheric temperature gradient in
211 controlling the timing of the onset of the Indian monsoon is well known (Li and Yanai 1996;
212 Goswami and Xavier 2005; Wu et al. 2012). In the lower troposphere, an anomalous low-

213 level cyclonic circulation cell was found over the northern Arabian Sea, coupled with an
214 anticyclonic cell over southeastern India and the southern Bay of Bengal (Fig. 2b).
215 Associated with these circulation cells were stronger low-level northeasterlies over the
216 Arabian Peninsular and strengthened low-level southwesterlies over the Arabian Sea and
217 westerlies over central India. The former would increase dust emission over the desert
218 surface, and the latter would increase dust and moisture transport from the Arabian Sea to
219 northern India. Strong anomalous cooling of the lower troposphere was found over the Indo-
220 Gangetic Plain (20-30^{o}N), and anomalous warming above with maximum upper troposphere
221 warming anchored over the Tibetan Plateau (Fig. 2c). These features were accompanied by
222 anomalous ascending motions and increased water vapor over the NIHF with sinking motion
223 and increased dryness over southern India, and northern Indian Ocean (Fig.2 c, d).
224 Increased monsoon westerlies were found in the lower troposphere over central and Northern
225 India, and enhanced easterlies, from the upper troposphere to near surface over the NIHF
226 (Fig. 2d). The aforementioned anomalies signal an enhancement of the early part of the
227 Indian monsoon consistent with the EHP effect due to dust aerosols (Lau et al. 2006, 2008;
228 Lau and Kim 2006). It should be noted that spring and summer of 2008 coincided with the
229 decay phase of the 2007-2008 La Nina, with significant anomalous cooling over the
230 equatorial central and eastern Pacific and warming of the southern tropical Indian Ocean
231 during the boreal spring and summer of 2008. These SST anomalies would have
232 significantly influenced the aforementioned anomalies of the Indian monsoon (Rao et al.
233 2010; Kim et al. 2015). However, given the prescribed observed SST in the control
234 experiment (NA), SST effects including possible impacts of aerosols on SST are already
235 included in the prescribed observed SST and lateral boundary conditions in NA. Hence

model differences (with respect to NA) will only be attributed to aerosol effects associated with aerosol-monsoon interaction on fast times scales, up to 7 days - the longest lead time chosen for the model forecast experiments.

3.*2 Impact on model forecasts*

Figure 3 compares the distribution of AOD, rainfall and 850 hPa winds in NA with observed rainfall from TRMM, AOD from MODIS, and winds from MERRA2 for the onset phase of the 2008 Indian monsoon (June 11-17). The NA experiment simulates the mean spatial distribution of aerosol AOD reasonably well compared to MODIS, featuring relatively high aerosol loading over the northern Arabian Sea, and northwestern Indo-Gangetic Plain, and low aerosol loading over northeastern India and the Bay of Bengal (Fig. 3). Overall, the AOD magnitude is underestimated, in some regions with only half the magnitude of MODIS AOD. An examination of the aerosol composition in GOCART has determined that a large-fraction of the AOD over the Arabian Sea and northwestern India and Pakistan is contributed mainly by desert dust (65-70%) transported from the Middle East deserts and the Thar desert of northwestern Indian subcontinent.

The model mean rainfall and wind patterns show broad similarities to observations (Fig. 3c, d), but with notable differences. The model low-level westerlies are too strong. As a result, precipitation upwind over the mountain ridges of the Western Ghats, and Indo-China are overestimated. The model also missed the heavy rainfall band extending from the east coast of northern India into the Bay of Bengal. These are mostly due to the excessive monsoon low-level westerlies across central and southern India. As shown in following discussion, these biases are not related to model aerosol physics, because they are essential

259 unchanged in the RAD and RADM simulations. Another notable feature is the excessive
260 model rainfall over the southern Indo-Gangetic Plain, and deficient rainfall over the HF
261 compared to TRMM. In the following, we will demonstrate how this bias is mitigated in the
262 RAD and RADM experiments and how we can use the incremental improvement to explore
263 the physical processes underlying aerosol-monsoon interactions over NIHF region. Despite
264 the aforementioned discrepancies, the overall AOD and rainfall distributions in the model are
265 consistent with dust aerosol emissions from the arid region of Southwest Asia, the Thar
266 desert, and Middle East deserts and transport across the Arabia Sea, with strong wet removal
267 in rainy regions.

268 Comparing the rainfall spatial distribution of RAD, and difference between RAD and
269 NA (Fig. 4a, b) depicts a shift of the monsoon rain band from NI to HF during the onset
270 phase, but little differences elsewhere. This means that given the large-scale aerosol and
271 meteorological initial condition, aerosol-monsoon interaction effects are mostly found over
272 the NIHF region. The latitudinal rainfall profile averaged over the 80-90^{o}E sector shows
273 clearly that the excessive NA model rainfall over the NI (23-25^{o}N), and deficient rainfall
274 over the HF (25-30^{o}N) compared to TRMM (Fig. 4c and d). ARI effects (Fig. 4e) clearly
275 shift the onset maximum rainfall northward towards the HF, mitigating but not completely
276 removing the model rainfall bias.

277 To further assess the impacts of aerosol-monsoon interactions on the model forecasts,
278 Fig. 5 shows the time series of the 1-7 days forecast rainfall, for NA and RAD, and TRMM,
279 for the extended integration period through 1 June to July 15 over the northern domain (ND),
280 and the southern domain (SD), defined along the curvature of the Himalaya mountain range
281 (see domain marker in Fig. 4b) to better capture the rainfall anomaly along the HF, arising

282 from aerosol-monsoon interaction. For the ND (Fig. 5a) the model forecasts show
283 reasonable skills in capturing the major episodes of heavy rainfall events. However, after the
284 onset, the model rainfall events tend to be overly active, with only much shallower breaks
285 compared to TRMM observations. It is also noted that clear differences between RAD and
286 NA forecasts tend to emerge after forecast day 3-4, when the control by the initial conditions
287 on the model forecasts are beginning to diminish. Beyond forecast day-4, the number of days
288 with predicted increased rainfall is much higher than that with reduced rainfall, in RAD
289 compared to NA, with a frequency ratio of approximately 2-to-1 indicating a strong impact
290 of absorbing aerosols in enhancing rainfall. The time series of the Day 5-7 mean forecasts
291 (Fig 5b) show clear enhanced rainfall in RAD relative to NA, during the on-set phase of
292 rainfall events, indicating an advance (~ 1-5 days) of the onset of monsoon rainfall over the
293 ND (Fig. 5c) due to ARI. The rainfall enhancement and advance of rain events in ND can be
294 seen to last through the entire month of June and to early July. Conversely over SD (Fig. 5c),
295 rainfall is reduced in RAD compared to NA. Beyond forecast day-4, the number of days
296 with reduced rainfall compared that with increased rainfall is approximately 9 to 1, as a result
297 of the northward shift of convection and rainfall away from the SD to the ND. Note that the
298 SD experiences reduction in rainfall mostly during the peak and more often during the
299 dissipation phase of the rainfall events (Fig. 5d).
300
301 *3.3 Large-scale interactions*
302 In this section, we explore aspects of aerosol-monsoon large-scale interaction, which
303 governs the northward shift of rainfall from the SD to the ND. The variations of anomalous
304 RAD rainfall and AOD are coherent (Fig. 6a), generally with enhanced rainfall in the ND

region (north of 27° N) where AOD is low, and suppressed rainfall in the regions of high AOD in the SD (south of 27° N). This is consistent with increased wash out of aerosols in wet regions, and longer aerosol life times in more stable dry regions. Wind anomalies (Fig. 6b) show a rapid strengthening and northward displacement of westerlies and southerlies in the SD accompanying the monsoon onset over the ND, starting around June 16. This is followed by a major event during June17-21 with increase in AOD, strengthening southwesteries in the SD coupled to enhanced rainfall in the ND. A similar event involving coherent variations of rainfall, AOD and winds took place during July 3-6. Note that anomalous low-level southerlies after the monsoon onset (~June 16) remain unchanged in sign, extending across approximately 27° N, from the SD to the ND. This means that the ambient moisture in the SD is being advected northward by the strengthened southerlies, thus increasing (decreasing) atmospheric moisture in the ND (SD). The resulting changes in convective stability in terms of the vertical profiles of moist static energy in the two regions will be discuss in Section 3.4. The aforementioned features indicate strong aerosol-monsoon interactions associated with advection of aerosols and increased precipitation downwind of the strengthening monsoon southwesterlies, consistent with EHP. The fluctuations in AOD, winds, and rainfall in the ND and SD are associated with development of westward propagating monsoon depression along the Himalayan foothills (See Section 3.4, for more detailed discussion). The overall aerosol radiation effects on the large-scale monsoon environment are examined next.

The RAD anomalies of upper tropospheric temperature and winds (Fig. 7a) shows clearly a warmer upper troposphere over northern India and regions further north with increased upper level easterlies are found near 18-25°N induced by ARI. The upper level

328 anomalies are coupled to a strengthened low-level monsoon southwesterlies and a
329 pronounced increase in moisture over northwest and northern India (Fig. 7b). Reduced
330 moisture associated with the dry air masses and desert dust transport is found over the central
331 Arabian Sea, and northeastern India. Except for the magnitude, the anomaly patterns are
332 quite similar to those shown in Fig. 2a and b. As stated previously, SST effects are already
333 included in the prescribed observed SST. The present experiments are focused only on the
334 fast responses of aerosol-monsoon dynamic interaction. The results here suggest that ARI
335 reinforces, and adds regional details to, the SST forcing.
336 Additional regional features induced by aerosol radiative effects are depicted in
337 meridional-height anomaly cross-sections (Fig. 8). Over the Arabia Sea (60-70E), the dust
338 aerosol layer is thick, extending from the surface to 600 hPa, with maximum concentration in
339 the 800-700 hPa layer (Fig. 8a). Pronounced atmospheric warming is found within the dust
340 layer, and cooling near the top of the dust layer mainly due to longwave radiation effects
341 (Zhang and Christopher 2003; Zhu et al. 2007; Lau et al. 2009). Substantial anomalous
342 warming is found over the upper troposphere 300-200 hPA layer, in conjunction with the
343 enhancement of the South Asian High and associated easterly warm advection (Fig. 7a).
344 Surface cooling is found over land surface north of 25^{o} N, reflecting solar attenuation effects
345 due to aerosols (Ramanathan et al. 2005). The differential warming/cooling in the vertical
346 increases stability in the lower troposphere, but enhances instability above, giving rise to
347 weak rising motion in the mid- troposphere (Fig. 8c). As a result, except near the center of
348 dust layer, the atmosphere over the Arabian Sea is generally moister (Fig. 8b). Given that
349 the same sea surface temperature is prescribed in all experiments, the source of moisture is
350 likely due to enhanced surface evaporation from the strengthened surface westerlies over the

351 Arabian Sea, as well as from increased mixing of the moist marine cloud water with
352 environmental air. Wind anomalies show increased easterlies (westerlies) in the upper
353 (lower) troposphere indicating a strengthening of the large-scale monsoon flow. The
354 colocation of low-level westerlies coincides with regions of maximum aerosol loading and
355 dry air masses signals strong westward advection of dust aerosols. As a result of the
356 aforementioned stability changes induced by ARI, an anomalous meridional circulation with
357 northward onshore flow towards southern Pakistan, and largely mid-tropospheric weak rising
358 motion is found over the region. This anomalous rising motion is likely to enhance
359 convective mixing and further moistening of the atmosphere over the ocean. However, the
360 region remains dry in the absolute sense, with no precipitation (Fig. 8d). Over the western
361 Indian region (70-80^{o}E), the aerosol-monsoon characteristics are similar to those over the
362 Arabian Sea except that the signals are stronger, including a clear northward shift of the
363 center of moderate precipitation, accompanying a strengthening of the local monsoonal
364 meridional circulation (Fig. S2).
365 The ARI effects on precipitation and circulation are strongest over the domain
366 covering eastern India and the western Bay of Bengal (80-90^{o} E). As shown in Fig. 8e, the
367 ARI-induced upper tropospheric warming over the Tibetan Plateau and regions to the south
368 are very pronounced. This occurs in conjunction with a pronounced elevated thick aerosol
369 layer, pushing against the southern slopes of the Tibetan Plateau by the increasing monsoon
370 southerlies (See Fig.6b). Here the dust loading is lower compared to that over the Arabian
371 Sea and western India, due to removal by both dry and wet depositions during the long-
372 distance transport from the Middle East deserts to eastern India. However, still noticeable
373 are the cooling near the top of the dust layer, warming within and below the dust layer and

374 near the surface, characteristic of light-absorbing dust layers [Zhu et al. 2007; Lau et al.
375 2009]. A signal of the aerosol semi-direct effect reducing convective potential, in the form
376 of strong surface cooling due to aerosol solar attenuation and warming induced by aerosol
377 heating can be found over the HF (25-35^{o} N, Fig. 8e). However, this effect is overpowered
378 by the increased low-level moisture advection into this region by the strengthened
379 southwesterlies, as evident in the increased moist static energy in the lower troposphere
380 (700hPa) relative to the regions above (See discussion in Section 3.4, Fig. 11). Except
381 within the dust layer, specific humidity is substantially increased over the entire atmospheric
382 column. The increase is most pronounced and coincides with a strong low-level westerly jet
383 near 25-30N, (Fig. 8f). Coupled to the wind, temperature, moisture and aerosol anomalies,
384 is an enhanced local meridional circulation, with strong rising motion in the HF, and sinking
385 motion to the south (Fig.8g), and the northward displacement of the maximum rainfall over
386 the HF (Fig. 8h).
387
388 *3.4 Mesoscale Interactions*
389 In this section, we present results on the mesoscale aspects of aerosol-monsoon
390 interactions including both ARI and ACI effects, based on comparisons of the RADM, RAD
391 and NA experiments. Here, we focus on the evolution of mesoscale development of
392 monsoon rainfall systems during the onset phase (June 11-17) of the 2008 Indian monsoon.
393 As shown in Fig. 9 (panels in left column), in the absence of aerosol effects (NA), the onset
394 of the Indian monsoon over northern India was associated with increased transport of
395 moisture to the NIHF regions by the increasing monsoon southwesterlies, resulting in the
396 spontaneous development of a monsoon depression (cyclonic circulation cell) over the

northern Bay of Bengal as shown in the NA Day-4 forecast. At Day-5, a secondary cyclone was spurred over the northern-central IGP. Subsequently, both monsoon cyclones amplified and propagated northwestward, over the IGP. Such evolution of monsoon depressions is well known during the monsoon onset, and active phases of the monsoon over northern India [Krishnamurti and Bhalme 1976; Saha et al. 1981]. In RAD (panels in middle column), the effect of ARI noticeable starting around Day-5, in a weakening of the primary monsoon depression compared to NA, and in the development of intense small-scale convection cells further northwestward up the HF. The suppression of the primary monsoon depression, and the development of vigorous convective cells along the HF continue, with the most pronounced signal at Day-7. In RADM (panels in right column), the inclusion of ACI further enhances the ARI effects (See discussions related to Fig. 10 and 11). The suppression of the primary monsoon onset cyclone is already noticeable at Day-4, and the subsequent transformation (Day-5 to Day-7) of the monsoon onset cyclones (in NA) is similar to ARI effects, except with faster speed, increased intensity and with more numerous convective cells. The metamorphosis of the monsoon depression in NA to invigorated line precipitation cells along the HF, due to combined effects of ARI and ACI is most striking at forecast Day-7.

The invigoration of deep convection by ARI and ACI in the HF region is further examined via the vertical distributions of hydrometeors associated with the deepening convection in the ND and SD. Without aerosol effects (NA), the distributions of liquid water (cloud and rain), cloud ice, snow and graupel indicate stronger development of deep convection in SD than in ND (Fig. 10a, b). Comparing RAD (Fig. 10c, d) with NA (Fig. 10a, b), ARI shifts the maximum cloud ice upwards from 250 hPa to 200 hPa, enhances the

420 concentration of snow and graupel in the 500-300 hPa layer, and increases liquid water
421 content in the lower troposphere in the ND. In the SD, the effects are reversed, with
422 substantial reduction in deep convection as evidenced in substantial loss of cloud ice, and
423 snow and graupel in the mid to upper troposphere, as well as suppressed cloud and rain water
424 in the lower troposphere. Comparing RADM (Fig. 10e, f) and RAD (Fig. 10c, d) anomalies
425 indicates that deep convection is further enhanced by ACI in ND, as evident in the larger
426 magnitude and extent of the increase in cloud ice, and snow/graupel in the mid- and upper
427 troposphere. This appears to be at the expense of reduced rate of increase in cloud and rain
428 water in the lower troposphere compared to RAD. In the SD, the stronger reduction
429 hydrometeors of all kinds suggest a further suppression of deep convection by ACI. For the
430 domain as a whole, the change in total rainfall due to inclusion of ACI is relatively small
431 (<5%). Most of the changes by ACI appear to be in the nature of the deep convection and
432 not in the total rain. These results are consistent with modeling and observations indicating
433 enhanced glaciation, and formation of deeper clouds by aerosols in a moist environment
434 [Rosenfeld *et al*. 2008, Fan *et al.* 2013].

435 The changes in the nature of the deep convection induced by ARI and ACI can be
436 viewed in terms of changes in moist static energy (MSE) of the atmosphere over the ND and
437 SD during the onset phase (Fig. 11). Judging from the stronger negative gradient (reduction
438 with height) in mean MSE in the lower troposphere (Fig. 11a, b), it can be inferred that in the
439 absence of aerosol influence (NA), the SD is more (compared to the ND) convectively
440 unstable, and convection is likely to be deeper, as reflected in the larger loading of
441 hydrometeors of all types (Fig. 10a, b). Under ARI forcing, the lower troposphere in ND
442 (Fig. 11c, d) is further destabilized with increase in negative gradient MSE between 800 hPa

443 and 600 hPa, while the mid- to upper troposphere between 600-300 hPa are stabilized, as
444 evidence in the positive gradients in MSE between these two levels. Above 300 hPa, the
445 MSE reflects again a convective de-stabilization of the atmosphere. Computations of
446 separate contributions to the MSE (Fig. S3) shows that the destabilization in the lower
447 troposphere is mainly due to increased moisture, while stabilization is mainly due to
448 temperature change, *i.e.*, aerosol semi-direct effect in heating the lower troposphere and
449 cooling of the surface. Changes in MSE in the mid-to upper troposphere is associated with
450 temperature change due to moist adiabatic ascent of heated air from below reaching
451 maximum altitude. Essentially, in the ND, the low-level moisture effect overpowers the
452 aerosol semi-effect, invigorating more intense convection and rainfall. Clearly, ACI
453 enhances the MSE convective stability modulation due to ARI, favoring enhanced deep
454 convection in ND (Fig. 11e). In contrast, for the SD under ARI (Fig. 11f), both the aerosol
455 semi-direct effect and the reduction in moisture by advection (see discussion related to Fig.
456 7) stabilizes the lower troposphere, leading to the dissipation of the monsoon depression and
457 suppressed precipitation. This effect is further amplified by ACI (Fig. 11f). As noted
458 previously, the northward advection of the un-precipitated moisture from suppressed rainfall
459 in SD by the strengthened southerlies can further increase in convective instability and
460 rainfall in ND. This is the essence of the EHP effect. Overall, it can be argued that the MSE
461 changes provide the physical underpinnings of anomalous deep convection, rainfall and
462 moisture transport induced by ARI and ACI in the NIHF region.
463

464 **4. Conclusions**

Using the NU-WRF model, we have conducted numerical forecast experiments to investigate the dynamics of aerosol-monsoon interaction over the complex topography of the NIHF region, under realistic initial and boundary conditions. Results show that aerosol-monsoon interactions have strong impacts on regional monsoon rainfall and circulation during the onset phase of 2008 Indian monsoon, consistent with the EHP hypothesis. Key findings include:

- The complex and steep topography of the Himalaya foothills facilitate the build up of thick layers of dust aerosols transported by monsoon southwesterlies from the Arabian Peninsular deserts across the Arabian Sea, and accumulated over northwestern and central India during the pre- and early monsoon season of 2008.
- Via aerosol induced dynamical feedback, ARI warms the upper troposphere over the Tibetan Plateau, increases the mid-to-upper tropospheric north-south temperature gradient, and thus strengthens the early Indian monsoon by shifting maximum monsoon rainfall from the Indo-Gangetic Plain to the Himalayan foothills regions, and advancing the timing of monsoon onset over HF by 1-5 days
- Aerosols have both local and non-local effects, which interacts with each other. Generally, regions of high aerosol loading are associated with drier air masses and suppressed rainfall, and heavy rain regions with low aerosol loading due to wash-out. The semi-direct (local) effect of dust aerosols leads to the stabilization and weakening of a developing monsoon depression over northeastern India and northern Bay of Bengal during the onset phase of the monsoon.
- Non-local effects are exerted mainly through moisture and circulation feedback. Heating by thick dust layer over the Arabian Sea and northern India, enhances the large-scale

488 southwesterly low-level monsoon flow and transport of moisture from the Arabian Sea to
489 the Indian subcontinent. The enhanced southwesterly moisture transport increases low-
490 level MSE, leading to the development of intense convective cells over the Himalaya
491 Foothill regions.

492 • While ARI dominates the large-scale aerosol-monsoon interaction, ACI further enhances
493 the ARI effects, by suppressing development of monsoon depression over northeastern
494 India, while intensifying the ice-phase precipitation and deep cloud processes in the HF,
495 and thereby speeding up the transformation the monsoon depression into intense meso-
496 scale cells with heavy rain in the forms line convection along the rugged terrains of the
497 HF.

498 Our results are in general agreement with recent modeling studies using the WRF-
499 CHEM. Krishnamurti *et al.* (2015) showed that the development of monsoon depression is
500 suppressed by aerosol via increased cloud condensation nuclei (CNN), over northeastern
501 India and Bay of Bengal. However, their results did not indicate development of mesoscale-
502 scale deep convection over the Himalayan foothills, most likely because aerosol number
503 concentration was prescribed in their experiments, which therefore did not include the full
504 interactions of aerosol radiation, microphysics, and removal processes, with monsoon
505 dynamics. Jin et al. (2015) using WRF-CHEM and satellite observations also found that the
506 influx of Middle East dust, mainly through radiative forcing, could redistribute and increase
507 Indian summer monsoon regional rainfall, consistent with our results. However the relative
508 low resolution model (~35 km) they used would be unable to resolve the aerosol-monsoon
509 dynamic interaction over the complex topography of Himalayas regions. Moreover, they
510 focused on the mean response of the entire Indian monsoon season (June- August), while we

emphasize the short-term (< 7days) interactions during the onset phase of the monsoon. We also note that, even with the 9-km resolution used our experiments, the resolution is still relative coarse, in terms of realistic representation of aerosol-cloud microphysics. Cloud resolving scales (< 2-3 km) is highly desirable for better representation the interaction of aerosol with the complex topography of the Himalaya foothills. However, for such high resolution simulation, only short-term integrations, with single or few ensemble simulations are feasible, because of the prohibitive computational demands. Furthermore, as noted in the discussion in Section 3.2, while NUWRF simulated the AOD spatial distribution reasonably well, the magnitude of the aerosol loading was significantly underestimated, compared to MODIS observation. Assuming that a heavier aerosol loading will produce stronger impacts on monsoon, it is plausible that the present results may have underestimated the actual impacts of aerosols in reality .

As a caveat, we note that our results are based on a singular monsoon year of 2008. More studies need to be carried out to ascertain the robustness of the results. Nonetheless, the fundamental physical processes revealed by this study, together with many recent studies of aerosol impacts on monsoon weather and climate, lend support to the paradigm that aerosol from natural sources is an essential components of the Asian monsoon climate, affecting variability of the monsoon on diverse spatio-temporal scales [Lau 2016]. Finally, an important message from our study, consistent with many contemporary studies on aerosol-monsoon interactions (See Li *et al*. 2016 for a comprehensive review), is *that aerosol-monsoon interaction is important not only for climate change but also for short-term weather (3-7 days) forecasts, and very likely for medium to long-term forecasts (> 7 days) as well as seasonal-to-interannual predictions of the Asian monsoon*.

Acknowledgement. This work is partially supported by the NASA Precipitating Measuring Mission (PMM) Program, the NUWRF project under NASA Modeling and Analysis and Prediction Program (MAP), and the Department of Energy/ Pacific Northwest National Laboratory Grant 4313671 to ESSIC, University of Maryland.

Reference

Andreae, M. O., and D. Rosenfeld, (2008), Aerosol–cloud–precipitation interactions. Part 1. The nature and sources of cloud-active aerosols. *Earth-Science Reviews*, **89**, 13–41.

Barros, A. P., and D. P. Lattenmaier (1994), Dynamic modeling of orographically induced precipitation, *Rev. Geophys*., 32, 265– 284.

Barros, A. P., and Timothy J. Lang (2003), Monitoring the Monsoon in the Himalayas: Observations in Central Nepal, June 2001. *Mon. Wea. Rev.*,**131**, 1408–1427.

Boos, W., and Z. Kuang (2010), Dominant control of the South Asian monsoon by orographic insulation versus plateau heating, *Nature, 463*, 218-222 doi:10.1038/nature08707.

Bosilovich, M. and coauthors (2015), MERRA-2: Initial Evaluation of the Climate., *Technical Report Series on Global Modeling and Data Assimilation, Ed. R. Koster,* NASA/TM-2015-104606/Vol.43.

Chin M., D. A. Chu, R. Levy, L. Remer, Y. Kaufman, B. Holben, T. Eck, P. Ginoux, and Q. Gao (2004), Aerosol distribution in the Northern Hemisphere during ACE-Asia: Results from global model, satellite observations, and Sun photometer measurements, *J. Geophys. Res*., 109, D23S90, doi:10.1029/2004GL02014.

Chin, M., T. Diehl, O. Dubovik, T. F. Eck, B. N. Holben, A. Sinyuk, and D. G. Streets (2009), Light absorption by pollution, dust and biomass burning aerosols: A global model study and evaluation with AERONET data, *Ann. Geophys*., 27, 3439-3464.

563 Chin, M., T. Diehl, Q. Tan, J. M. Prospero, R. A. Kahn, L. A. Remer, H. Yu, A. M.
564 Sayer, H. Bian, I. V. Geogdzhayev, B. N. Holben, S. G. Howell, B. J. Huebert, N.
565 C. Hsu, D. Kim, T. L. Kucsera, R. C. Levy, M. I. Mishchenko, X. Pan, P. K.
566 Quinn, G. L. Schuster, D. G. Streets, S. A. Strode, O. Torres, and X.-P. Zhao
567 (2014), Multi-decadal variations of atmospheric aerosols from 1980 to 2009 : a
568 perspective from observations and a global model, *Atmos. Chem. Phys*., 14, 3657-
569 3690.
570 Collier and G. J., Zhang (2009)Aerosol direct forcing of the summer Indian monsoon as
571 simulated by the NCAR CAM3. *Clim Dyn* 32: 313. doi:10.1007/s00382-008-
572 0464-9
573 D'Errico, M., C. Cagnazzo, P. G. Gogli, et al., 2015: Indian monsoon and the elevated-
574 heat pump mechanism in a coupled aerosol-climate model. *J. Geophys. Res*., 120,
575 8712–8723, doi:10.1002/2015JD023346.
576 Das, S., U. C. Mohanty, A. Tyagi, D. R. Sikka, P. V. Joseph, L. S. Rathore, A. Habib, S.
577 K. Baidya, K. Snam and A. Sarkar (2014), The SAARC STORM: A
578 coordinated filed experiment on severe Thunderstorm obsevations and regional
579 modeling over the South Asian region. *Bull. Am. Meteor. Soc*., 603-617,
580 DOI:10.1175/BAMS-D-12-00237.1
581 Demott, P. J., A. J. Prenni, X. Liu, S. M. Kreidenweis, M. D. Petters, C. H. Twohy, M. S.
582 Richardson, T. Eidhammer , and D. C. Rogers (2010), Predicting global
583 atmospheric ice nuclei distributions and their impacts on climate. *Proc. Natl.*
584 *Acad. Sci.*, **107 (25)**, 11217–11222.

585 Eck, T. F., et al. (2010), Climatological aspects of the optical properties of fine/coarse
586 mode aerosol mixtures, *J. Geophys. Res.*, 115, D19205,
587 doi:10.1029/2010JD014002.
588 Fan, J., L. R. Leung, D. Rosenfeld, Q. Chen, Z. Li, J. Zhang, and H. Yan (2013),
589 Microphysical effects determine macrophysical response for aerosol impacts on deep
590 convective clouds, *Proc. Natl. Acad. Sci. U. S. A.*, *110*, E4581–90,
591 doi:10.1073/pnas.1316830110.Gadgil, S., et al. (2003), The Indian monsoon and its
592 variability precipitation fluctuations in the Nepal Himalaya and its vicinity and
593 relationship with some large-scale climatological parameters, *Annu. Rev. Earth*
594 *Planet. Sci*., 31, 429– 467
595 Ganguly, D., H. Gadhavi, A. Jayaraman, T. A. Rajesh, and A. Misra (2005), Single
596 scattering albedo of aerosols over the central India: Implications for the regional
597 aerosol radiative forcing, *Geophys. Res. Lett.*, *32*, doi:10.1029/2005GL023903.
598 Gillette, D. A., and R. Passi (1988), Modeling dust emission caused by wind eroson *J.*
599 *Geophys. Res.*, 93, 14233-14242.
600 Ginoux, P., M. Chin, I. Tegen, J. M. Prospero, B. Holben, O. Dubovik, and S.-J.
601 Lin (2001), Sources and distributions of dust aerosols simulated with the
602 GOCART model, *J. Geophys. Res.*, 106(D17), 20255–20273,
603 doi:10.1029/2000JD000053.
604 Goswami, B. N., and P. K. Xavier (2005), ENSO control on the south Asian monsoon
605 through the length of the rainy season, *Geophys. Res. Lett.*, 32, L18717,
606 doi:10.1029/2005GL023216.

607 Hazra, A., B. N. Goswami, and Jen-Ping Chen, 2013: Role of Interactions between Aerosol
608 Radiative Effect, Dynamics, and Cloud Microphysics on Transitions of Monsoon
609 Intraseasonal Oscillations. *J. Atmos. Sci.*, **70**, 2073–2087.
610 doi: http://dx.doi.org/10.1175/JAS-D-12-0179.1
611 Henriksson, S. V., J.-P. Pietikäinen , A.-P. Hyvärinen , P. Räisänen , K. Kupiainen, J.
612 Tonttila, R. Hooda , H. Lihavainen, D. O'Donnell , L. Backman , Z. Klimont , and
613 A. Laaksonen (2014), Spatial distributions and seasonal cycles of aerosol climate
614 effects in India seen in a global climate–aerosol model, *Atmos. Chem. Phys*., 14,
615 10177–10192, 2014 www.atmos-chem-phys.net/14/10177/2014/ doi:10.5194/acp-
616 14-10177-2014
617 Houze, R. A., Wilton, D. C. and Smull, B. F. (2007), Monsoon convection in the Himalayan
618 region as seen by the TRMM Precipitation Radar. *Quart. J. Roy. Meteor. Soc.*,
619 133: 1389–1411. doi: 10.1002/qj.106
620 Jin, Q., J. Wei1 , Z.-L. Yang, B. Pu , and J. Huang (2015), Consistent response of Indian
621 summer monsoon to Middle East dust in observations and simulations, Atmos.
622 Chem. Phys., 15, 9897–9915, doi:10.5194/acp-15-9897-2015
623 Kim, M.-K., W. K.-M. Lau, K.-M. Kim, et al., 2015: Amplification of ENSO effects on
624 Indian summer monsoon by absorbing aerosols. *Climate Dyn*., 1–15, doi:
625 10.1007/s00382-015-2722-y.
626 Koehler, K. A., S. M. Kreidenweis, P. J. DeMott, A. J. Prenni, C. M. Carrico, B. Ervens,
627 and G. Feingold (2006), Water activity and activation diameters from
628 hygroscopicity data — Part II: Application to organic species. *Atmos. Chem.*
629 *Phys.*, **6**, 795–809.

Krishnamurti, T. N., Xue, J., Bedi, H. S., Ingles, K. and Oosterhof, D. (1991), Physical initialization for numerical weather prediction over the tropics. *Tellus* B, 43: 53–81. doi: 10.1034/j.1600-0889.1991.t01-2-00007.x

Krishnamurti, T. N., and H. Bhalme (1976), Oscillations of a monsoon system. Part I: Observational aspects. *J. Atmos. Sci*., 33, 1937–1954.

Krishnamurti T.N., A. Martin, R. Krishnamurti, A.Simon, A. Thomas, V. Kumar (2013), Impacts of enhanced CCN on the organization of convection and recent reduced counts of monsoon depressions. *Clim. Dyn*. 41:117-134, doi 10.1007/s00382-012-1638-z.

Lang, S., W.-K. Tao, J.-D. Chern, D. Wu, and X. Li (2014), Benefits of a 4th ice class in the simulated radar reflectivities of convective systems using a bulk microphysics scheme, *J. Atmos. Sci.,***71**, 3583-3612.

Lau, W. K. M. (2016), The Aerosol-Monsoon Climate System of Asia: A New Paradigm. *J. Meteor. Res.*, 29(6), doi: 10.1007/s13351-015-5999-1.

Lau, W. K. M. (2014), Desert Dust and Monsoon Rainfall, *Nature, Geoscience* doi:10.1038/ngeo2115

Lau, K. M., and K. M. Kim (2006), Observational relationships between aerosol and Asian monsoon rainfall, and circulation, *Geophys. Res. Lett*.. 33, L21810, doi:10.1029/2006GL027546.

Lau, K. M., Kim, K. M., Sud, Y. C., and Walker, G. K. (2009), A GCM study of the response of the atmospheric water cycle of West Africa and the Atlantic to

652 Saharan dust radiative forcing, *Ann. Geophys.*, 27, 4023-4037, doi:10.51941
653 Angeo-27-4023-2009.
654 Lau, K. M., M. K. Kim, and K. M. Kim (2006), Aerosol induced anomalies in the Asian
655 summer monsoon: The role of the Tibetan Plateau. *Climate Dynamics*, **26** (7-8),
656 855-864, doi:10.1007/s00382-006-0114-z.
657 Lau, K.M, V. Ramanathan, G-X. Wu, Z. Li, S. C. Tsay, C. Hsu, R.Sikka, B. Holben, D.
658 Lu, G. Tartari, M. Chin, P .Koudelova, H. Chen, Y. Ma, J. Huang, K. Taniguchi,
659 and R. Zhang.(2008) the Joint Aerosol-Monsoon Experiment: A New Challenge
660 in Monsoon Climate Research. *Bull. Am. Meteor. Soc*., **89**, 369-383,
661 DOI:10.1175/BAMS-89-3-369.
662 Li, C., and M. Yanai (1996), The onset and interannual variability of the Asian summer
663 monsoon in relationship to land-sea thermal contrast. *J. Climate,* 9, 358-374.
664 Li, Z., W.K.-M. Lau, V. Ramanathan, G. Wu Y. Ding, M.G. Manoj, J. Liu, Y. Qian, J. Li,
665 T. Zhou, J. Fan, D. Rosenfeld, Y. Ming, Y. Wang, J. Huang B. Wang, X. Xu, S.-
666 S., Lee, M. Cribb, F. Zhang, X. Yang, T. Takemura, K. Wang, X. Xia, Y. Yin, H.
667 Zhang, J. Guo, P.M. Zhai, N. Sugimoto, S. S. Babu· G.P. Brasseur. (2016),
668 Aerosol and Monsoon Climate Interactions over Asia. *Geophys. Rev*. (in press).
669 Liu, Y., and P. H. Daum (2004), Parameterization of the autoconversion process. Part I:
670 Analytical formulation of the Kessler-type parameterizations. *J. Atmos. Sci*, **61**,
671 1539-1548.Manoj, M. G., P. C. S. Devara, P. D. Safai (2011), Absorbing aerosols
672 facilitate transition of Indian monsoon breaks to active spells. *Climate Dyn*.,
673 37,2181–2198, doi:10.1007/s00382-010-0971-3.

674 Meehl, G., J. Arblaster, and W. Collins (2008), Effects of black carbon aerosols on the
675 Indian monsoon, *J. Climate*, *21*, doi:10.1175/2007JCLI1777.1.
676 Peters-Lidard, C.D., E. M. Kemp, T. Matsui, J. A. Santanello, Jr., S. V., Kumar, J. P.
677 Jacob, T. Clune, W.-K. Tao, M. Chin, A. Hou, J. L. Case,, D. Kim, K.-M. Kim,
678 W. Lau, Y. Liu, J.-J. Shi, D. Starr, Q. Tan,, Z. Tao, B. F. Zaitchik, B. Zavodsky,
679 S. Q. Zhang, M. Zupanski (2015), Integrated modeling of aerosol, cloud,
680 precipitation and land processes at satellite-resolved scales, *Environmental*
681 *Modelling & Software*, **67**, 145-159
682 doi:http://dx.doi.org/10.1016/j.envsoft.2015.01.007
683 Peters-Lidard, P. R. Houser, Y. Tian, S. V., Kumar, J. Geiger, S. Olden, L. Lighty, B.
684 Doty, P. Dirmeyer, J. Adams, K. Michell, E. F. Wood, J. Sheffield (2007), High-
685 performance earth system modeling with NASA/GSFC's Land Information
686 System (LIS), *Innovations in Systems and Software Engineering*, 3, 157-165,
687 DOI:10.1007/s11334-007-0028-x.
688 Ramanathan, V., C. Chung, D. Kim, T. Bettge, L. Buja, J. T. Kiehl, W. M. Washington,
689 Q. Fu, D. R. Sikka, and M. Wild (2005), Atmospheric brown clouds: Impacts on
690 South Asian climate and hydrological cycle, *Proc. Natl. Acad. Sci. USA*, *102*, 5326-
691 5333, doi:10.1073/ pnas.0500656102.
692 Randles, C. A., and V. Ramaswamy (2008), Absorbing aerosols over Asia: A
693 Geophysical Fluid Dynamics Laboratory general circulation model sensitivity study
694 of model response to aerosol optical depth and aerosol absorption, *J. Geophys. Res.*,
695 *113*, doi:10.1029/2008JD010140.

696 Rao, S. A., H. S. Chaudhari, S. Pokhrel, and B. N. Goswami (2011), Unusual central Indian
697 drought of summer monsoon 2008: Role of Southern Tropical Ocean Warming, *J.*
698 *Climate,* 23, 5163-5174, DOI:10.1175/2010JCL3257.1
699 Rasmussen, K. L., and R.A. Houze Jr. (2012), A Flash-Flooding Storm at the Steep Edge of
700 High Terrain: Disaster in the Himalayas. *Bull. Amer. Meteor. Soc.*, **93**, 1713–1724.
701 Rosenfeld, D., U. Lohmann, G. B. Raga, C. D. O'Dowd, M. Kulmala, S. Fuzzi, A. Reissell,
702 and M. O. Andreae (2008), Flood or drought: how do aerosols affect precipitation?,
703 *Science*, *321*, doi:10.1126/science.1160606.Saha, K., F. Sanders, J. Shukla (1981),
704 Westward propagating predecessors of monsoon depressions. *Mon. Wea. Rev.,* 109,
705 330-343.
706 Sanap, S. D., and G. Pandithurai. (2015), The effect of absorbing aerosols on Indian
707 monsoon circulation and rainfall: A review. *Atmospheric Research*.
708 Satheesh, S. K., K. Krishna Moorthy, S. Suresh Babu, V. Vinoj, and C. B. S. Dutt (2008),
709 Climate implications of large warming by elevated aerosol over India, *Geophys. Res.*
710 *Lett.*, *35*, doi:10.1029/2008GL034944.
711 Shi, J. J., T. Matsui, W.-K. Tao, C. Peters-Lidard, M. Chin, Q. Tan, K. Pickering, N.
712 Guy, S. Lang, and E. Kemp (2014), Implementation of an Aerosol-Cloud
713 Microphysics-Radiation Coupling into the NASA Unified WRF: Simulation
714 Results for the 6-7 August 2006 AMMA Special Observing Period. *Quart. J. Roy.*
715 *Meteor. Soc.*, **140**, 2158-2175, doi:10.1002/qj.2286
716 Tao, W.-K., D. Anderson, J. Chern, J. Estin, A. Hou, P. Houser, R. Kakar, S. Lang, W.
717 Lau, C. Peters-Lidard, X. Li, T. Matsui, B.-W. Shen, J.-J. Shi, and X. Zeng, 2009:

718 Goddard Multi-Scale Modeling Systems with Unified Physics, *Annales*
719 *Geophysics*, **27**, 3055-3064.
720 Tao, W.-K., J.-P. Chen, Z. Li, C. Wang, and C. Zhang (2012), Impact of aerosols on
721 convective clouds and precipitation, *Rev. Geophys*., 50, RG2001,
722 doi:10.1029/2011RG000369.
723 Tao, Z., J. A. Santanello, M. Chin, S. Zhou, Q. Tan, E. M. Kemp, and C. D. Peters-Lidard
724 (2013), Effect of land cover on atmospheric processes and air quality over the
725 continental United States – a NASA Unified WRF (NU-WRF) model study, Atmos.
726 Chem. Phys., 13, 6207–6226.Tyagi, A., H. R. Hatwar and D. S. Pai, 2009: Monsoon
727 2008: A Report. National Climate Centre, *Indian Met. Dept., Monograph,*
728 *Synoptic Meterorology* No: 07/2009
729 Vinoj, V., P. J. Rasch, H. L. Wang, et al. (2014), Short term modulation of Indian
730 summer monsoon rainfall by West Asian dust. *Nat. Geosci*., **7**, 308–313,
731 doi:10.1038/NGEO2107
732 Wang, C., D. Kim, A. M. L. Ekman, M. C. Barth, and P. J. Rasch (2009), Impact of
733 anthropogenic aerosols on Indian summer monsoon, *Geophys. Res. Lett*., 36,
734 L21704, doi:10.1029/2009GL040114.
735 Wu, G., Y Liu, B. He, Q. B, A. Duan, F. F. Jin, (2012), Thermal controls on the Asian
736 Summer Monsoon, *Sci. Reports*, 404, doi:10.1038/srep00404
737 Zhang, J., and S. A. Christopher (2003), Longwave radiative forcing of Saharan dust
738 aerosols estimated from MODIS, MISR, and CERES observations on
739 Terra*, Geophys. Res. Lett.,* 30, 2188, doi:10.1029/2003GL018479, 23.

740 Zhu, A., V. Ramanathan, F. Li, and D. Kim (2007), Dust plumes over the Pacific, Indian,
741 and Atlantic oceans: Climatology and radiative impact, *J. Geophys. Res*., 112,
742 D16208, doi:10.1029/2007JD008427.
743

744 **Figure Caption**

745 Figure 1 Spatial distribution of observed a) rainfall anomalis (mm day^{-1}) from TRMM
746 and b) AOD from MODIS, for the Indian monsoon during June 2008. Rainfall
747 anomalies are computed related to 1998-2013 climatology.

748 Figure 2 Horizontal distribution of anomalies of a) tropospheric temperature (^oC) and
749 winds (ms^{-1}) averaged between 500-200 hPa , b)850 hPa winds and specific
750 humidity (gKg^{-1}) in the lower troposphere (1000-600hPa; and latitude-height
751 cross-sections of c) meridional overturning circulation (streamline) and
752 temperature, and d) zonal winds (contour) and specific humidity.

753 Figure 3 Horizontal distribution of AOD a) in control model simulation (NA), and b)
754 from MODIS observation. Rainfall and winds in c) NA experiment, and b) from
755 TRMM, and MERRA2. Unit of rainfall in mm day^{-1}, and winds in ms^{-1}.

756 Figure 4 Distribution of a) total rainfall in RAD, b) rainfall anomalies in RAD.
757 Latitudinal profile of rainfall averaged between 80-90 E in c) TRMM
758 observations, d) NA, and e) RAD, with positive (negative) RAD-minus-NA
759 differences indicated by red (blue) shading. The boundaries of Northern and
760 Southern Domain defined based on local tropograhy used for later analysis are
761 also shown.

762 Figure 5 Time series of a) individual 7-day rainfall forecasts June 10-July 21 and b)
763 ensemble mean of Day5-Day7 forecasts for the Northern Domain, and same for
764 c) and d) except for the Southern Domain (See domain definition in Fig 4b).
765 Histogram in a) and c) indicates observed TRMM rainfall in the Northern Domain

766 and the Southern domain respectively. Red (blue) dots and shading indicate
767 enhanced (reduced) rainfall in RAD relative to NA. Unit of rainfall in $mmday^{-1}$.
768 Figure 6 Latitude-time cross-section of ensemble mean forecasts during June 1- 17, 2008
769 for a) AOD (contour) and rainfall anomalies (in % change), and b) zonal wind
770 (shaded) and meridional wind (contour). Unit of wind in ms^{-1}.
771 Figure 7 Horizontal distribution of RAD anomalies in a) temperature averaged between
772 500-200 hPa and 200 hPa winds, and b) lower tropospheric moisture and winds
773 during June 10-17, 2008.
774 Figure 8 Height-latitude cross sections of a) temperature (color shaded) and AOT
775 (contoured), b) specific humidity (color shaded) and zonal wind (contoured), c)
776 meridional streamlines with vertical upward (downward) motions shaded red
777 (blue), and d) precipitation anomalies for the Arabian Sea-Pakistan-Afghanistan
778 region (60-70E). Positive (negative) anomalies are indicated by solid (dashed)
779 contours, or red (blue) color. Same for e), f), g) and h), except for the northern
780 and northeastern India sector.
781 Figure 9 Time sequence showing the genesis and evolution of monsoon rainfall and
782 mesoscale convective complex from forecast Day4 to Day 7, for a) NA, b) RAD
783 and c) RADM. Extreme heavy precipitation (> 120 mm day^{-1}) is shaded red.
784 Figure 10 Time-height distribution of different hydrometeor species for a) the Northern
785 Domain in NA, and b) the Southern Domain in NA. Same for c) and d), except
786 for the RAD anomalies, and same for e) and f), except for RADM anomalies.
787 Purple contour, color shading, and black contour denotes respectively
788 concentration of cloud-ice, snow and graupel, and liquid phase clouds and rain.

789 Positive (negative) anomalies in c) through f) are indicated either by solid
790 (dashed) contours or red (blue) shading. Units are in 10^{-5} kg m $^{-3}$.
791 Figure 11 Vertical profile of MSE (KJ Kg^{-1}) showing a) mean distribution for the
792 Northern Domain and b) the Southern Domain. Same for c) and d) except for
793 RAD anomalies for forecast Day 6, and e) and f) except for RADM anomalies for
794 forecast Day 6.

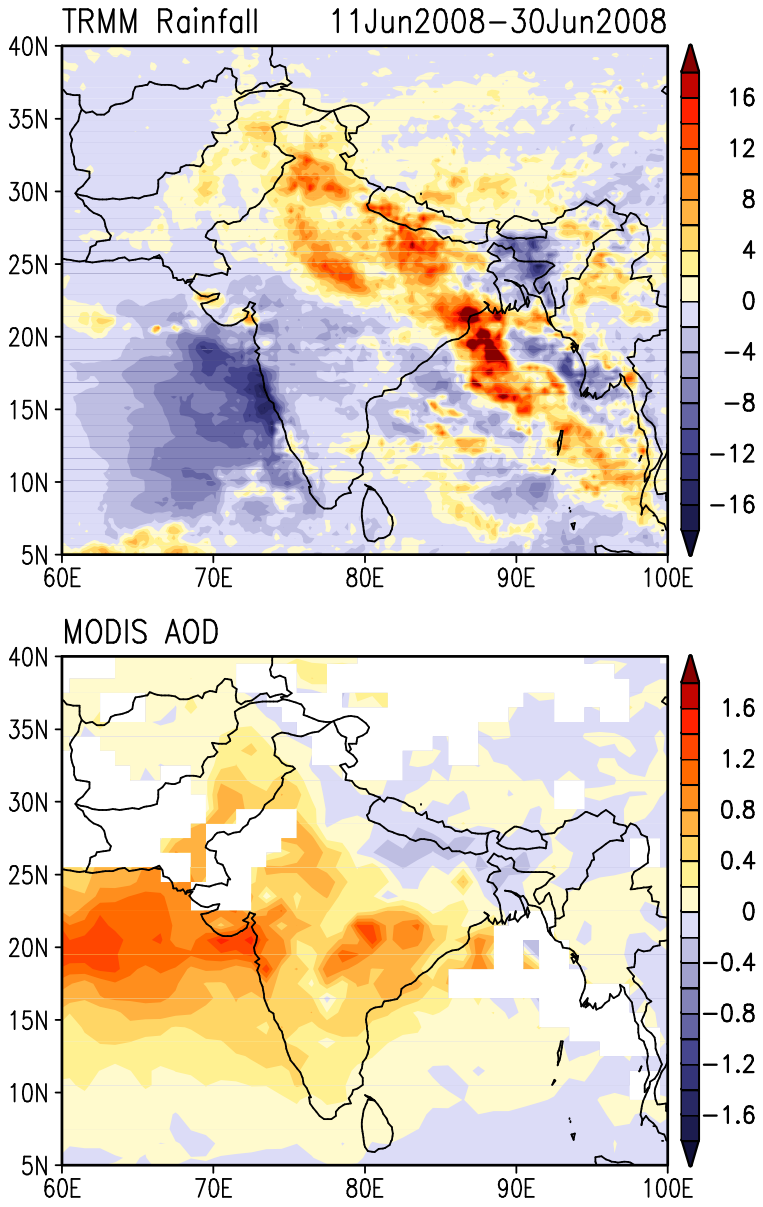

Figure 1 Spatial distribution of observed a) rainfall anomalis (mm day^{-1}) from TRMM and b) AOD from MODIS, for the Indian monsoon during June 2008. Rainfall anomalies are computed related to 1998-2013 climatology.

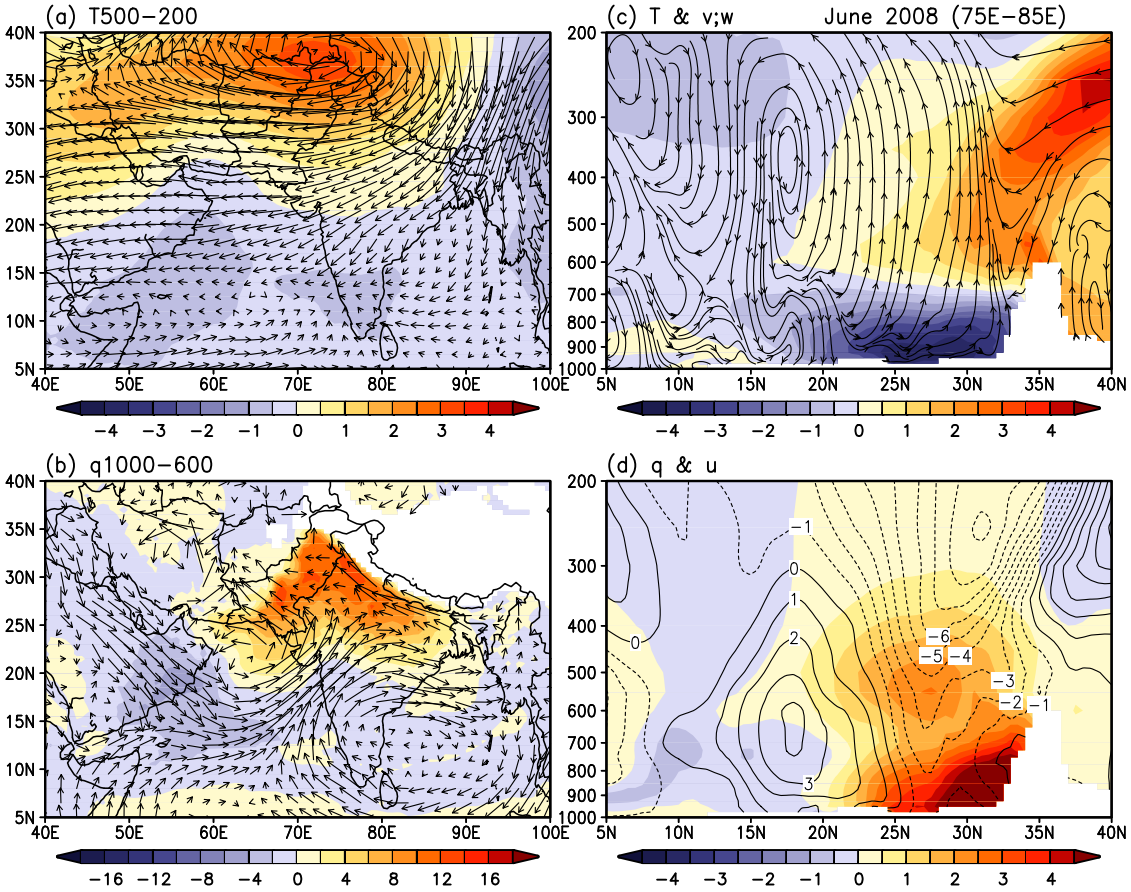

Figure 2 Horizontal distribution of anomalies of a) tropospheric temperature (°C) and winds (ms^{-1}) averaged between 500-200 hPa , b)850 hPa winds and specific humidity (gKg^{-1}) in the lower troposphere (1000-600hPa; and latitude-height cross-sections of c) meridional overturning circulation (streamline) and temperature, and d) zonal winds (contour) and specific humidity.

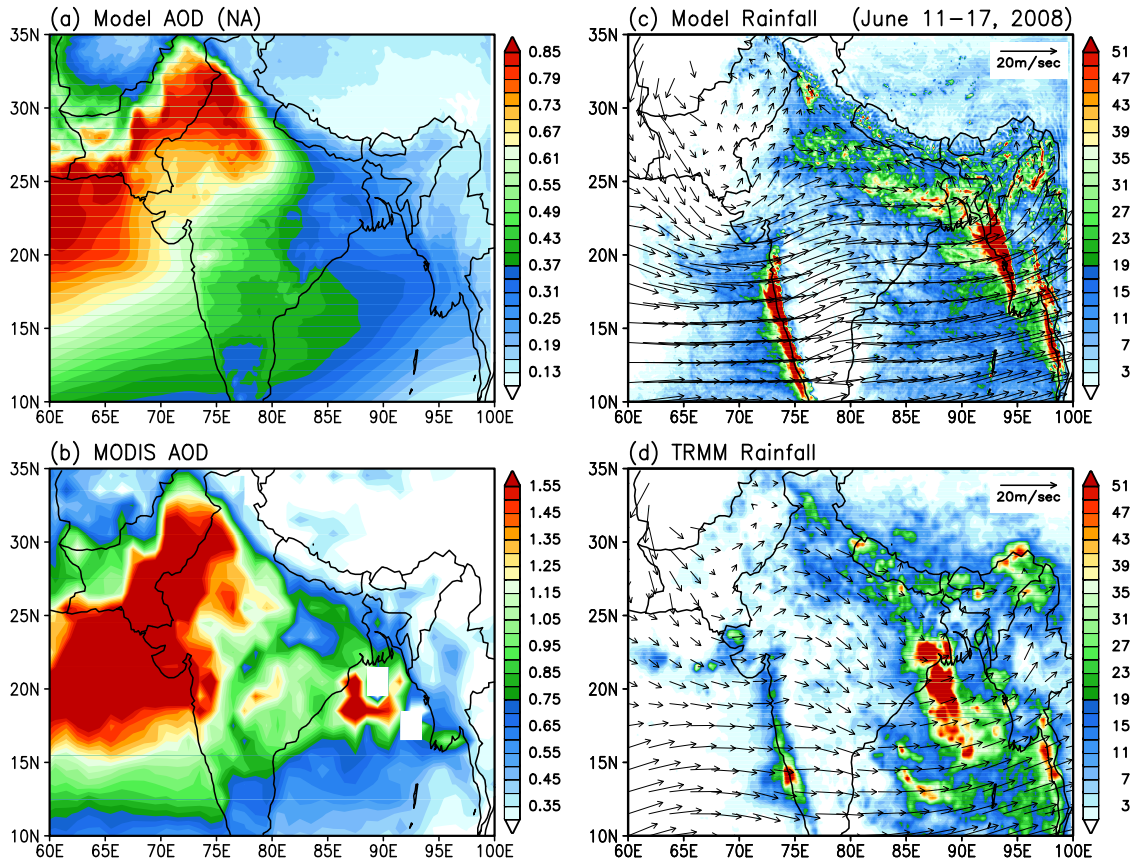

Figure 3 Horizontal distribution of AOD a) in control model simulation (NA), and b) from MODIS observation. Rainfall and winds in c) NA experiment, and b) from TRMM, and MERRA2. Unit of rainfall in mm day^{-1}, and winds in ms^{-1}.

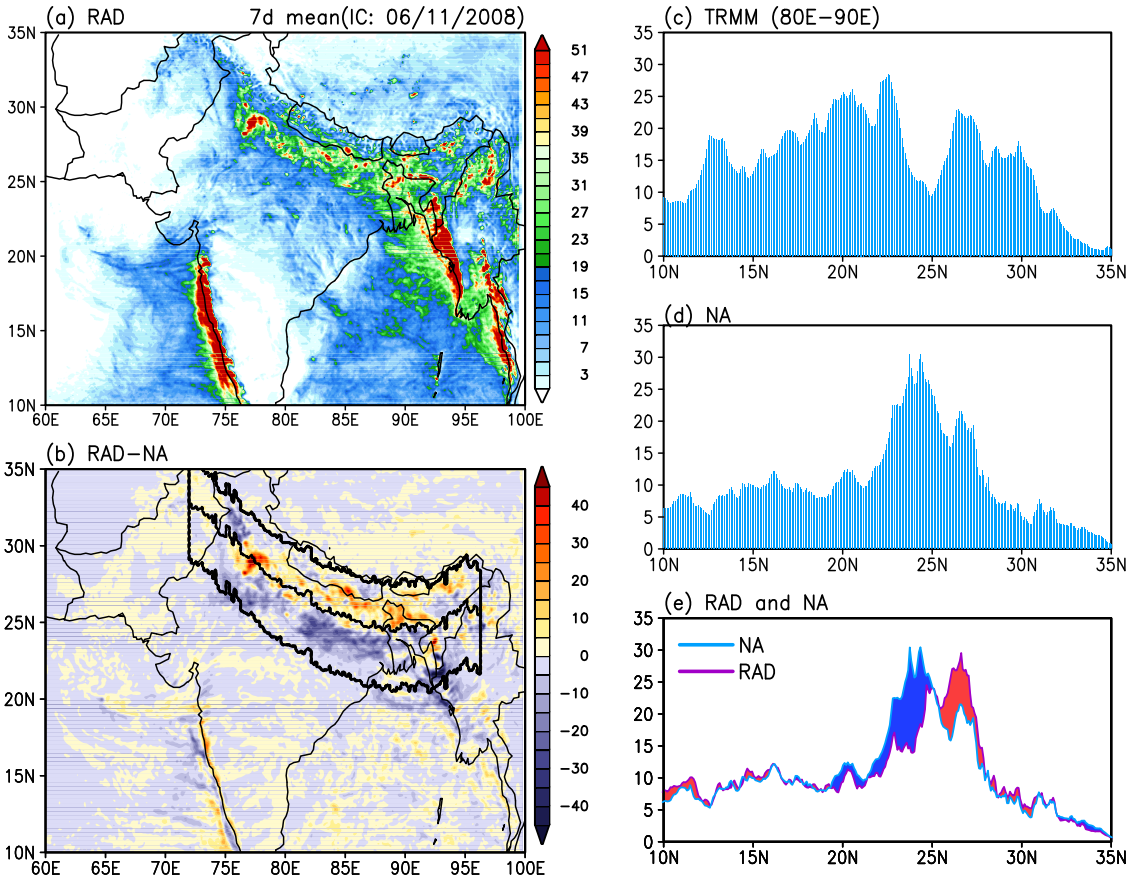

Figure 4 Distribution of a) total rainfall in RAD, b) rainfall anomalies in RAD. Latitudinal profile of rainfall averaged between 80-90 E in c) TRMM observations, d) NA, and e) RAD, with positive (negative) RAD-minus-NA differences indicated by red (blue) shading. The boundaries of Northern and Southern Domain defined based on local tropograhy used for later analysis are also shown.

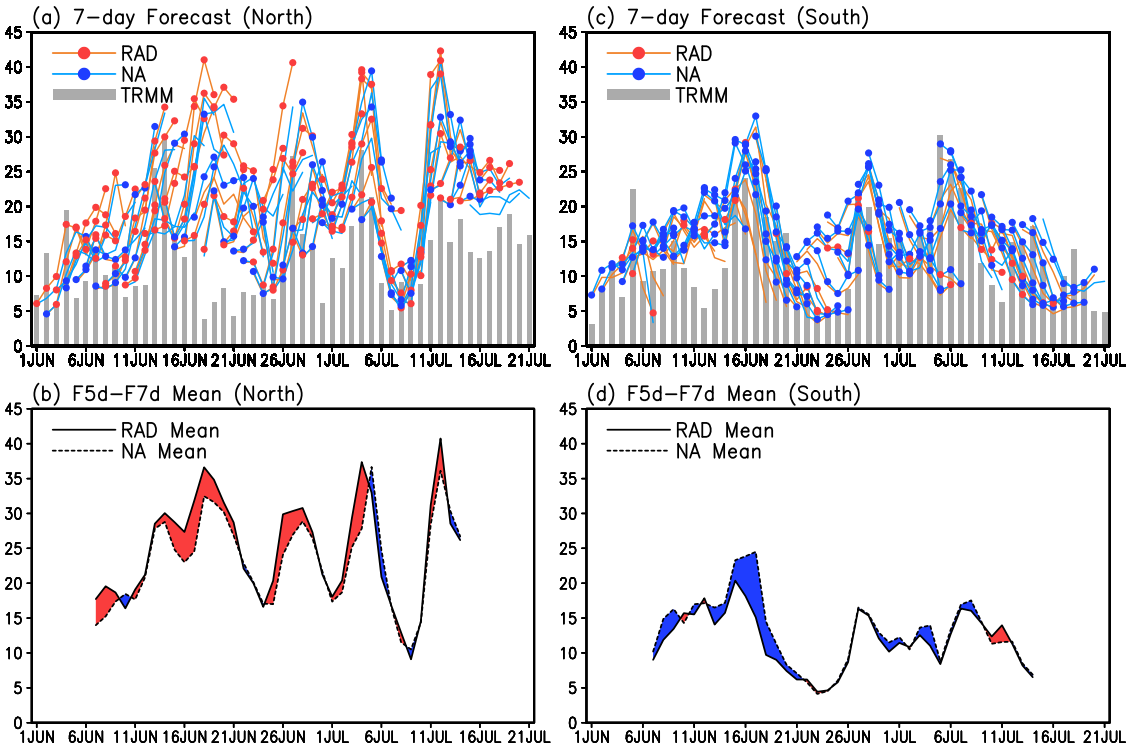

Figure 5 Time series of a) individual 7-day rainfall forecasts June 10-July 21 and b) ensemble mean of Day5-Day7 forecasts for the Northern Domain, and same for c) and d) except for the Southern Domain (See domain definition in Fig 4b). Histogram in a) and c) indicates observed TRMM rainfall in the Northern Domain and the Southern domain respectively. Red (blue) dots and shading indicate enhanced (reduced) rainfall in RAD relative to NA. Unit of rainfall in $mmday^{-1}$.

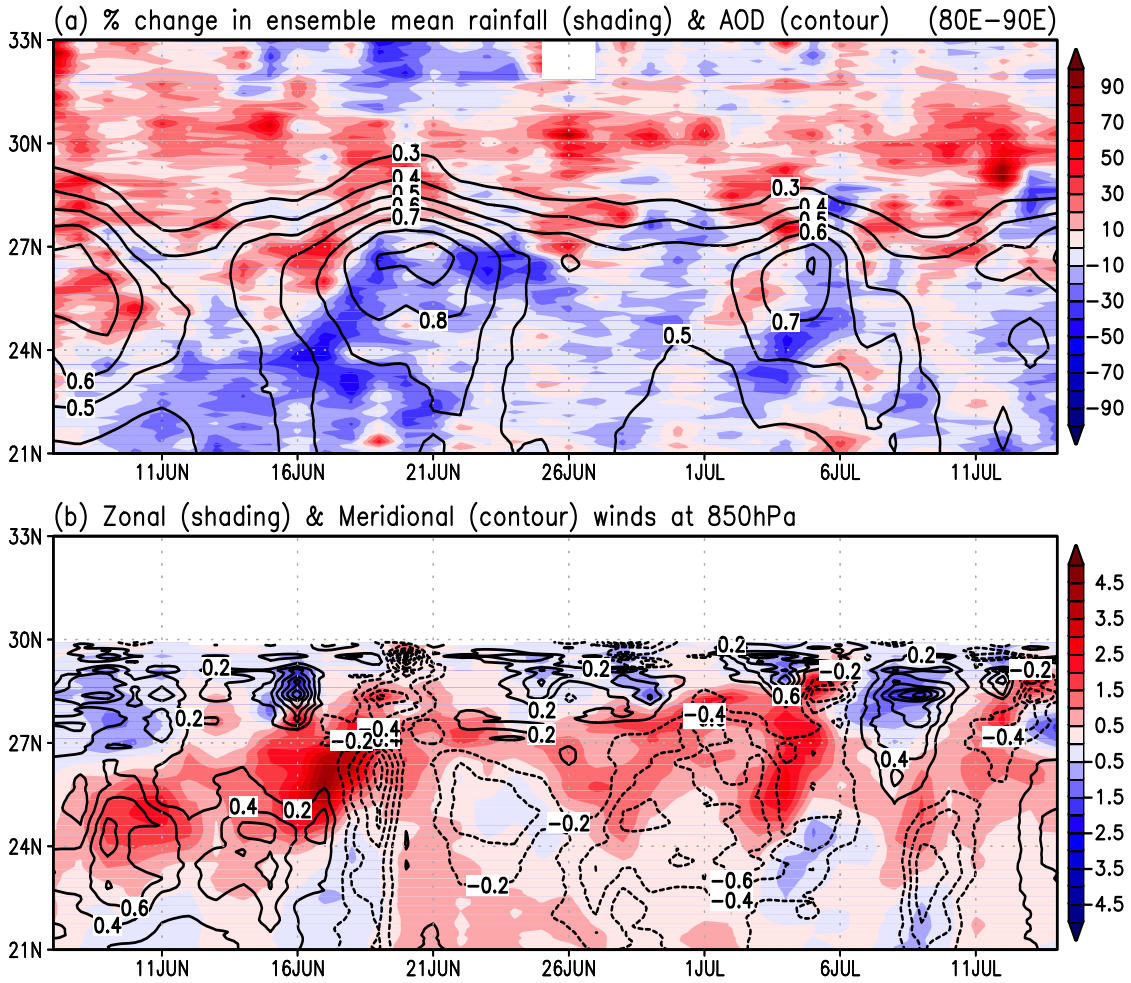

Figure 6 Latitude-time cross-section of ensemble mean forecasts during June 1- 17, 2008 for a) AOD (contour) and rainfall anomalies (in % change), and b) zonal wind (shaded) and meridional wind (contour). Unit of wind in ms^{-1}.

875

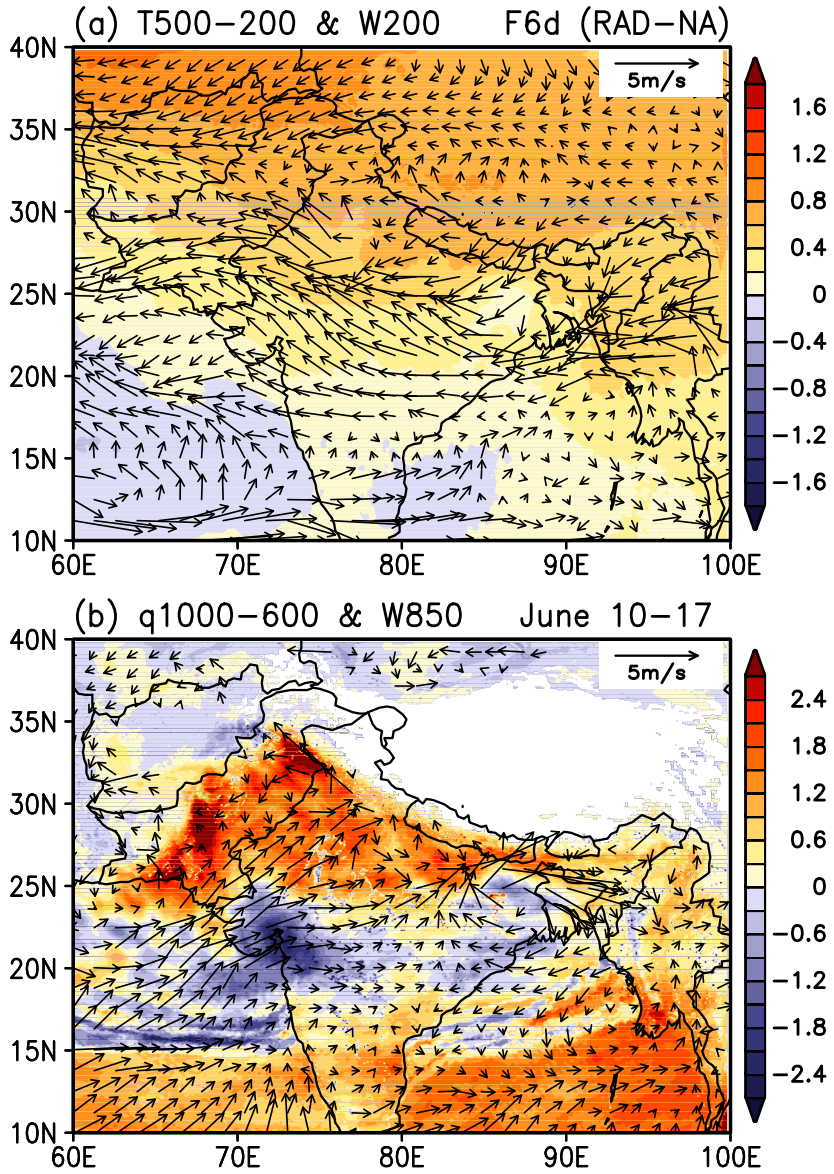

876

877 Figure 7 Horizontal distribution of RAD anomalies in a) temperature averaged between
878 500-200 hPa and 200 hPa winds, and b) lower tropospheric moisture and winds
879 during June 10-17, 2008.
880

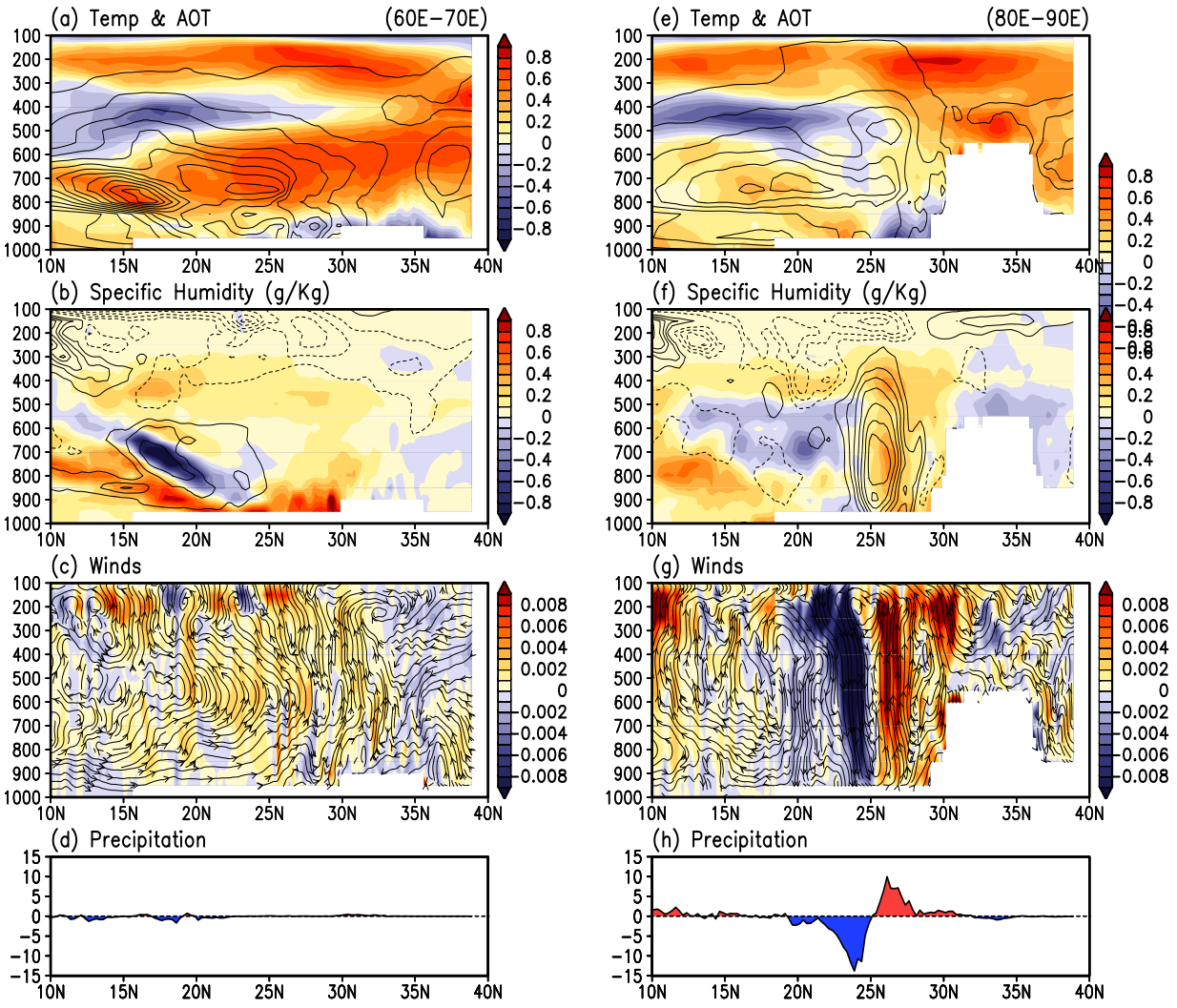

Figure 8 Height-latitude cross sections of a) temperature (color shaded) and AOT (contoured), b) specific humidity (color shaded) and zonal wind (contoured), c) meridional streamlines with vertical upward (downward) motions shaded red (blue), and d) precipitation anomalies for the Arabian Sea-Pakistan-Afghanistan region (60-70E). Positive (negative) anomalies are indicated by solid (dashed) contours, or red (blue) color. Same for e), f), g) and h), except for the northern and northeastern India sector.

893 Figure 9
894

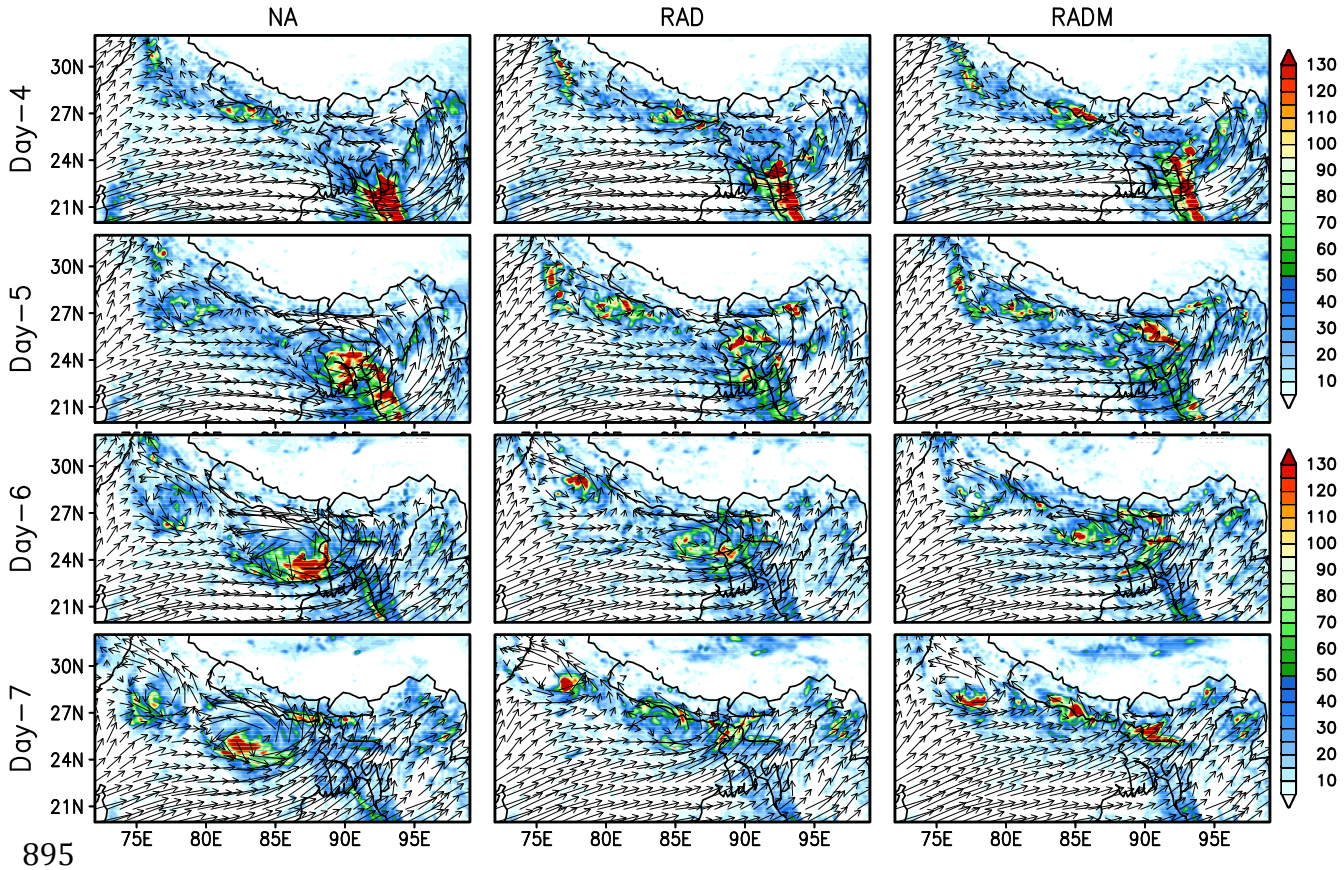

895
896
897 Figure 9 Time sequence showing the genesis and evolution of monsoon rainfall and
898 mesoscale convective complex from forecast Day4 to Day 7, for a) NA, b) RAD
899 and c) RADM. Extreme heavy precipitation (> 120 mm day^{-1}) is shaded red.
900
901

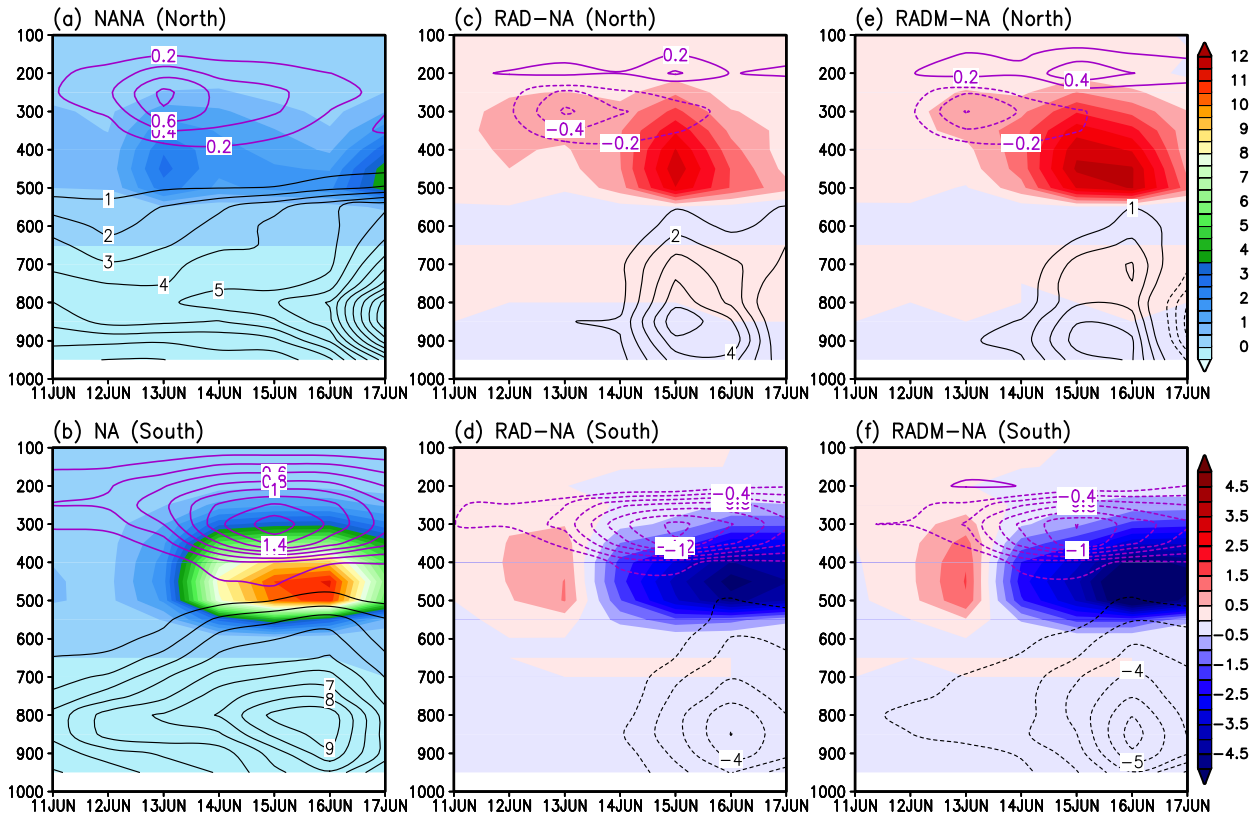

Figure 10 Time-height distribution of different hydrometeor species for a) the Northern Domain in NA, and b) the Southern Domain in NA. Same for c) and d), except for the RAD anomalies, and same for e) and f), except for RADM anomalies. Purple contour, color shading, and black contour denotes respectively concentration of cloud-ice, snow and graupel, and liquid phase clouds and rain. Positive (negative) anomalies in c) through f) are indicated either by solid (dashed) contours or red (blue) shading. Units are in 10^{-5} kg m $^{-3}$.

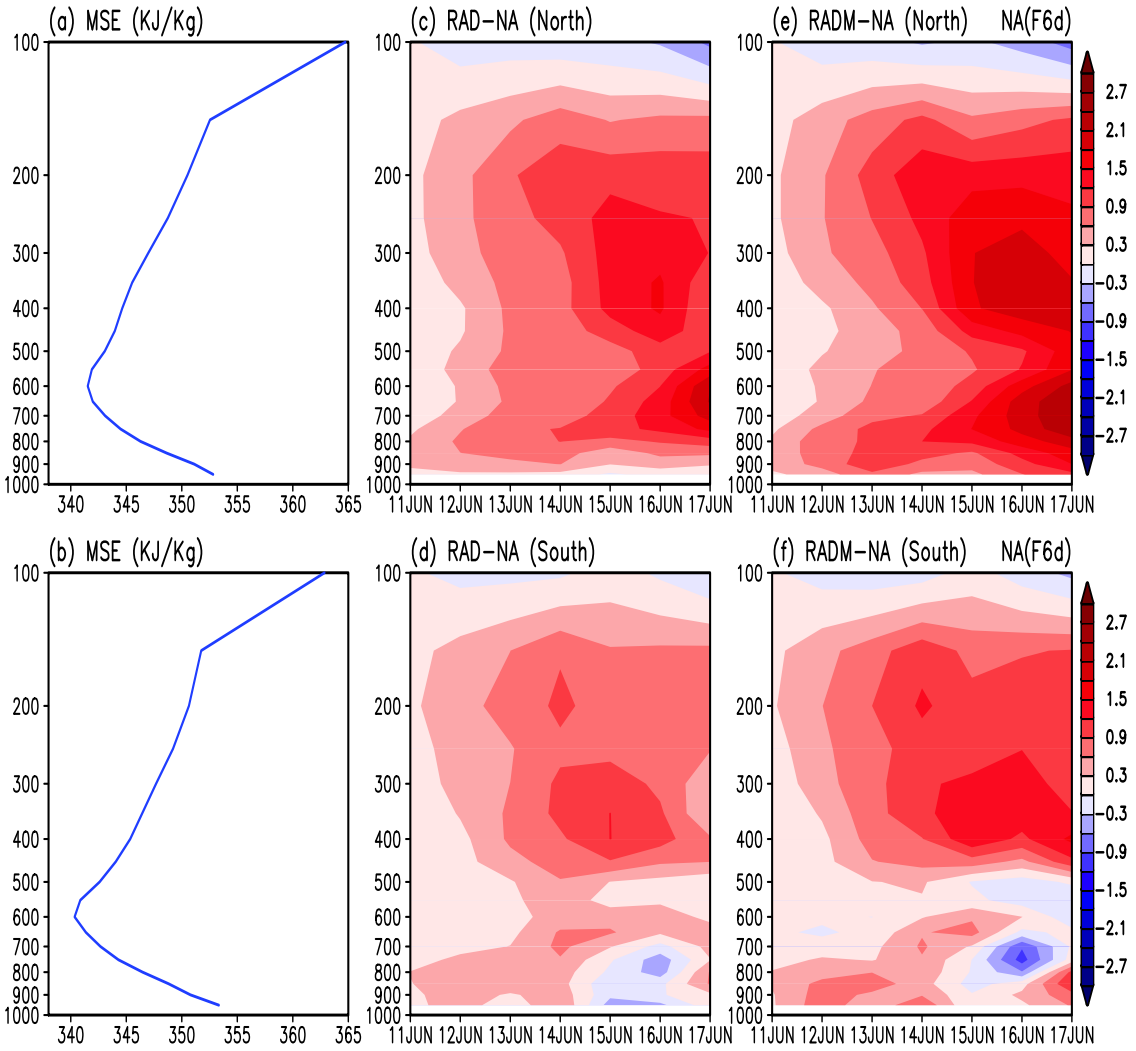

Figure 11 Vertical profile of MSE (KJ Kg^{-1}) showing a) mean distribution for the Northern Domain and b) the Southern Domain. Same for c) and d) except for RAD anomalies for forecast Day 6, and e) and f) except for RADM anomalies for forecast Day 6.

Supplementary Material

Figure S1 Nested domains used for NUWRF numerical experiments in this study. The horizontal resolution is 9 x 9 km , and 27x27 km for the inner domain and the outer domain respectively.

Figure S2 Height-latitude cross sections of a) temperature (color shaded) and AOT (contoured), b) specific humidity (color shaded) and zonal wind (contoured), c) meridional streamlines with upward (downward) motions shaded red (blue), and d) precipitation anomalies for the Arabian Sea-Pakistan-Afghanistan region (70-80^{o} E). Positive (negative) anomalies are indicated by solid (dashed) contours, or red (blue) color.

Figure S3 Vertical profile of MSE anomalies for a) the Northern Domain and b) the Southern Domain at forecast Day-6. Same for c) and d) except for contribution by temperature, and for e) and f) except for contribution by moisture.

941

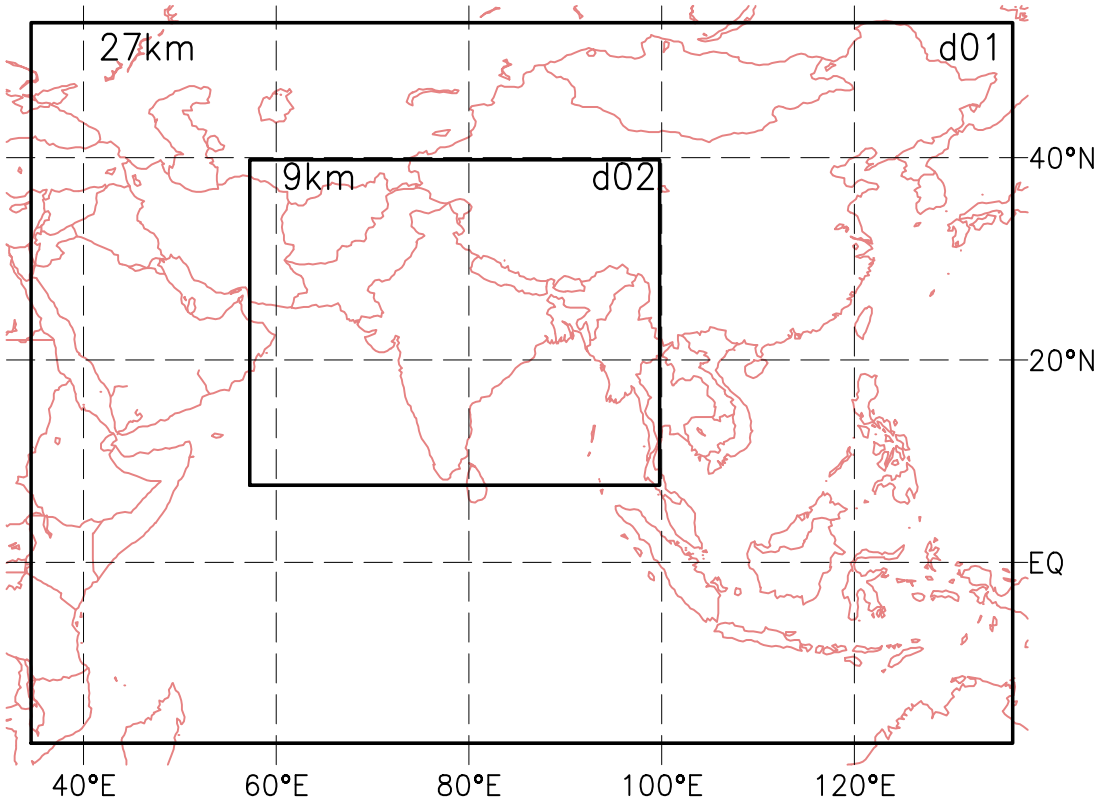

942

943 Figure S1 Nested domains used for NUWRF numerical experiments in this study.
944 The horizontal resolution is 9 x 9 km , and 27x27 km for the inner domain
945 and the outer domain respectively.
946

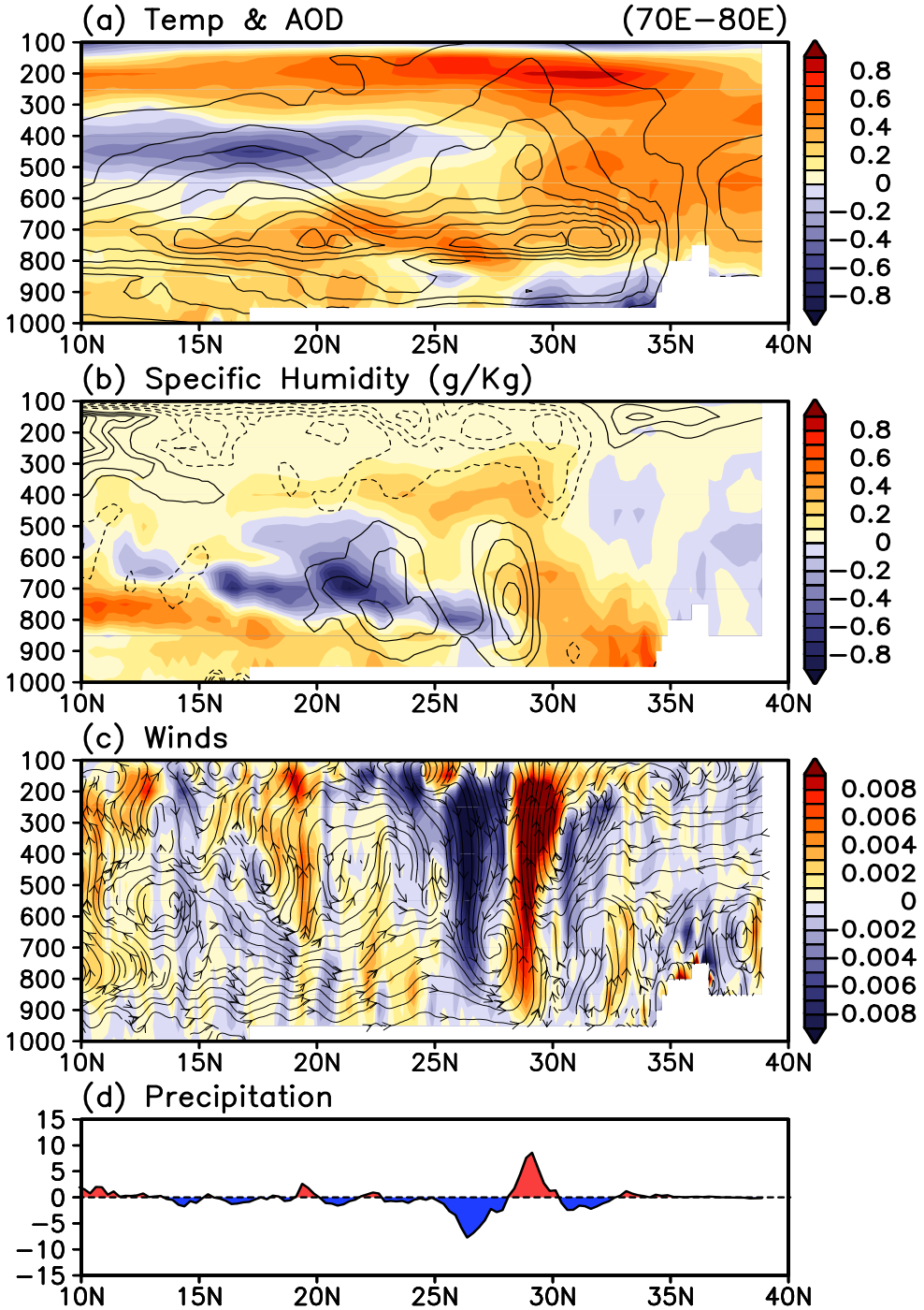

947

948 Figure S2 Height-latitude cross sections of a) temperature (color shaded) and AOT
949 (contoured), b) specific humidity (color shaded) and zonal wind (contoured), c)
950 meridional streamlines with upward (downward) motions shaded red (blue), and
951 d) precipitation anomalies for the Arabian Sea-Pakistan-Afghanistan region (70-
952 80° E). Positive (negative) anomalies are indicated by solid (dashed) contours, or
953 red (blue) color.

954

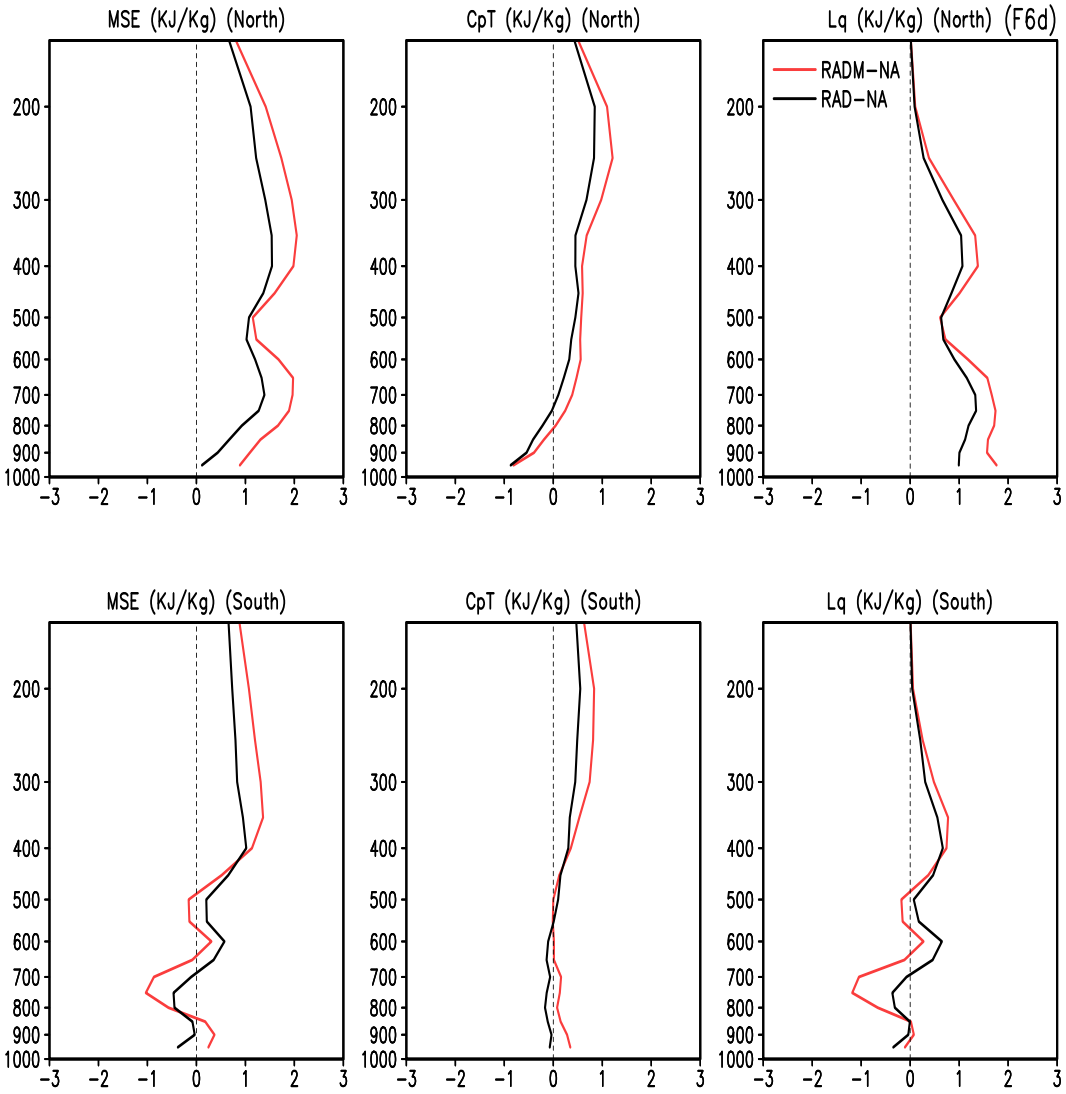

955

956 Figure S3 Vertical profile of MSE anomalies for a) the Northern Domain and b) the
957 Southern Domain at forecast Day-6. Same for c) and d) except for contribution
958 by temperature, and for e) and f) except for contribution by moisture.
959

960